Excitons in CdSe quantum dots

U. E. H. Laheld
Institutt for Fysikk, Norges Teknisk-naturvitenskapelige Universitet, N-7034 Trondheim, Norway

G. T. Einevoll*
Institutt for Matematiske Realfag, Nordlysobservatoriet, Universitetet i Tromsø, N-9037 Tromsø, Norway
(Received 19 July 1996)

Recent advances in material synthesis have provided samples with CdSe quantum dots with a degree of monodispersity high enough to allow for observation of excited exciton states and their size dependence [Norris *et al.*, Phys. Rev. Lett. **72**, 2612 (1994)]. Here we report theoretical results for these exciton states using the effective bond-orbital model (EBOM) for the hole and single-band effective-mass theory (EMT) for the electron in an iterative Hartree scheme including the Coulomb interaction and finite offsets. We present results for hole energies, exciton energies, and exciton oscillator strengths and compare with experiments and other theoretical results. Our results are found to account for most of the important features of the experimental absorption spectra by Norris *et al.* In particular, experimental states corresponding to the exciton ground state $(1\Gamma_8-1S_e)$, as well as the $2\Gamma_8-1S_e$ and $3\Gamma_8-1S_e$ excited states, have been identified. Also, a set of experimental exciton states observed lifted with an energy close to the spin-orbit splitting $\lambda\approx 420$ meV above the exciton ground state have been identified as Γ_7-1S_e spin-orbit split-off states with large oscillator strengths. A nonperturbative study of the effects of the crystal-field splitting, which is inherent in hexagonal CdSe quantum dots, revealed patterns of avoided crossings, accompanied with redistribution of oscillator strengths, between different exciton states for increasing values of the crystal-field splittings. In CdSe where the crystal-field splitting is ≈ 25 meV, the splitting is not expected to have a significant effect on the present quantum dot absorption spectra. [S0163-1829(97)06008-6]

I. INTRODUCTION

Quantum confinement effects of excitons in quantum dots have been studied intensely in the past few years.[1,2] In quantum dots excitons may be confined in all spatial dimensions, and if the exciton Bohr radius is comparable to the quantum dot size, quantum confinement effects can be observed. A variety of types of quantum dots have been investigated experimentally and/or theoretically. They include CdS, ZnS, CuCl, CuBr, CdS, CdSe, CdTe, and GaAs quantum dots which usually are embedded in a large band-gap matrix such as glass, rocksalt, polymers, zeolites, or liquids.

Due to sample inhomogeneities such as distributions in size and shape, the discrete nature of the exciton states is usually not seen, and only the blueshift of the exciton ground state due to confinement is observed. In the present theoretical study we focus on CdSe quantum dots.[3–12] The reason is that advances in material synthesis for this material system have provided samples with CdSe quantum dots with a degree of monodispersity which is high enough to allow also for observation of excited exciton states and their size dependence.[12] Moreover, self-organization of CdSe quantum dots into three-dimensional quantum dot superlattices has recently been demonstrated.[13]

Different theoretical models have been used in the study of quantum dots. They include single-band effective-mass theory (EMT),[14–16] spherical multiband effective-mass theory (SMEMT),[11,17–22] the empirical tight-binding method,[23,24] the empirical pseudopotential method,[25,26] and the effective bond-orbital model (EBOM).[27–31] Both SMEMT (Ref. 11) and EBOM (Ref. 31) have been used previously to study excited exciton states in CdSe quantum dots.

The SMEMT method was introduced by Baldereschi and Lipari,[17,18] who rewrote the Kohn-Luttinger Hamiltonian[32] for the hole as a sum of terms with spherical and cubic symmetries. In SMEMT only the spherical terms are kept. Ekimov *et al.*[11] used the SMEMT to calculate the energy levels for excitons in spherical quantum dots. Both the light-hole, heavy-hole, and split-off valence bands were accounted for. The electron and hole energies were calculated independently, and for the electron levels a Kane model[33] was used. Both the electron and the hole offsets were assumed infinite, and the Coulomb interaction was added only as a first-order perturbation.

The main advantage with the SMEMT compared to other numerically demanding methods (e.g., the multiband effective-mass method, the tight-binding methods, and the EBOM) is that the hole energies are found by determining roots of transcendental equations.[34] However, in the applications of the SMEMT to excitons in CdSe quantum dots reported so far, several simplifications have been made. First, the SMEMT introduces an artificially high symmetry compared to the symmetry of the hexagonal (or cubic) CdSe lattice. This results in an artificially high degeneracy of the energy states. Second, the assumption that the band offsets for the electron and the hole are infinite is probably not an adequate approximation in most materials (including CdSe quantum dots). For finite offsets the exciton wave function will penetrate into the barrier material, and this leads to lower confinement energies than for infinite offsets. For excited states where the wave functions are less localized, one

must expect that the magnitude of the offsets will be particularly important. Third, the independent calculations of electron and hole energies, which neglect the influence of the Coulomb interaction on the exciton wave function, are only expected to provide a good approximation when the quantum dot radius is small compared to the exciton Bohr radius. For larger quantum dots the Coulomb interaction between the electron and hole should be included nonperturbatively.

In this study we calculate exciton energies and oscillator strengths in CdSe quantum dots using the EBOM for the hole and the EMT for the electron in an iterative Hartree scheme which incorporates the Coulomb interaction nonperturbatively in the calculations. The calculational scheme readily includes finite electron and hole offsets. An additional attractive feature of our scheme is that it allows for studies of the effect of the crystal-field term[35] due to the hexagonal lattice in wurtzite CdSe (Refs. 12 and 36) on the exciton energy spectrum and the corresponding oscillator strengths.

The EBOM is used for the hole since in hexagonal CdSe the light-hole and heavy-hole valence bands are nearly degenerate at the zone center so that a single-band effective-mass approach is insufficient to give quantitatively correct results. The basic idea of EBOM is to use a minimum number of bond orbitals to describe the most relevant portion of the band structure for the bulk materials. Both the light-hole, the heavy-hole, and the split-off valence bands are included in the calculations. In EBOM the interaction parameters are fitted to the experimentally observed bulk band structure around the zone center and are given in terms of the Luttinger parameters used in the SMEMT. As a consequence, EBOM (and SMEMT) predict much wider hole bands than what is experimentally observed.[27] EBOM can be viewed as a discretized version of effective-mass theory and thus represents a link between the multiband effective-mass approach and the empirical tight-binding method.

In Ref. 31 Ramaniah and Nair reported interesting EBOM results on CdSe quantum dots. They used interaction parameters which grossly reproduced the main features of the bulk band structure. However, only infinite offsets were considered, and the Coulomb interaction was not included in the Hamiltonian. While the parametrization scheme in Ref. 31 may be advantageous for very small quantum dots, we use the standard fitting scheme[27] in the present study since this scheme ensures agreement with multiband effective-mass theory for larger quantum dots.

The organization of the rest of the paper is as follows. In Sec. II the calculational method is outlined. In Sec. III we discuss how the material parameters for CdSe are chosen. In Sec. IV the hole energy spectra and, in particular, the effect of the crystal-field term are investigated. In Sec. V we calculate exciton energy spectra and oscillator strengths for CdSe and compare the results with experiments as well as other theoretical work. Some concluding remarks are given in Sec. VI.

II. CALCULATIONAL METHOD

In the first part of this section we review the iterative Hartree scheme used in this work for calculating the exciton energies. In the second part the form of the electron wave function is given and in the subsequent part the form of the hole wave function is chosen by group-theoretical arguments. In the last part expressions for calculating the oscillator strengths are given. We will, however, only outline the calculational schemes used in this study, since they are similar to schemes used in work reported earlier.[28,29,37,38] These references should be consulted for details. In Ref. 28 acceptor states in semiconductors and quantum dots were investigated, in Ref. 37 excitons bound to isoelectronic impurities in bulk ZnSe and in ZnSe-$Zn_{1-x}Mn_xSe$ quantum wells were studied, and in Ref. 29 excitons in CdS quantum dots were considered.

A. The iterative Hartree scheme

Our model Hamiltonian H for the exciton is given by

$$H = H_h(\nabla_h, \mathbf{r}_h) + H_e(\nabla_e, \mathbf{r}_e) + v(|\mathbf{r}_h - \mathbf{r}_e|), \tag{1}$$

where H_h (H_e) is the Hamiltonian for the hole (electron) in the quantum dot potential, and $v(|\mathbf{r}_h - \mathbf{r}_e|)$ is the attractive Coulomb potential between the electron and the hole. The exciton energies are found by minimizing

$$\frac{\langle \Psi(\mathbf{r}_e, \mathbf{r}_h)|H|\Psi(\mathbf{r}_e, \mathbf{r}_h)\rangle}{\langle \Psi(\mathbf{r}_e, \mathbf{r}_h)|\Psi(\mathbf{r}_e, \mathbf{r}_h)\rangle} = E, \tag{2}$$

in a self-consistent Hartree scheme. We assume a separable wave function

$$\Psi_{l,m}(\mathbf{r}_e, \mathbf{r}_h) = \psi_{e,l}(\mathbf{r}_e)\psi_{h,m}(\mathbf{r}_h). \tag{3}$$

Here $\psi_{e,l}(\mathbf{r}_e)$ $(\psi_{h,m}(\mathbf{r}_h))$ denotes the wave function for the lth (mth) energy state of the electron (hole). This approximation is expected to be particularly suitable in the so-called strong confinement regime where the electron and hole can be regarded as nearly independent particles. This requires a sufficiently small dot radius R and sufficiently large electron and hole offsets. In the present application on CdSe quantum dots we consider dots with radii of the order of the exciton Bohr radius a_B^* and smaller. In order to test whether the Hartree procedure gives reasonable results for dots of this size, we have performed a simple model computation. In single-band EMT we calculated the ground-state energy of an exciton in a quantum dot with infinite offsets and with a radius $R = a_B^*$. For equal effective masses we obtained $6.237E_{\mathrm{Ry}}^*$. This is 4.4% higher than the result $5.974E_{\mathrm{Ry}}^*$ of an extensive variational calculation[15] with the same parameters. For smaller R the agreement is even better.

Let us also mention that for infinite offsets using single-band EMT for both the electron and the hole Kayanuma[15] estimated that R had to be smaller than about $2a_B^*$, in order to be in the strong confinement regime. In this regime the ground-state exciton energy E is given by

$$E/E_{\mathrm{Ry}}^* = \pi^2\left(\frac{a_B^*}{R}\right)^2 - 3.572\frac{a_B^*}{R} - 0.248, \tag{4}$$

where E_{Ry}^* is the exciton Rydberg energy. In Ref. 29, where the present combined EBOM-EMT scheme was used on CdS quantum dots, it was confirmed that the separable wave function gives infinite-offset ground-state energies in good agreement with the last two terms in Eq. (4) for $R < 2a_B^*$ We thus

expect the use of a separable wave function to be a good approximation particularly for the lower-lying exciton states with large offsets.

Insertion of the separable wave function (3) into Eq. (2) yields

$$\frac{\langle\psi_{h,m}|H_h|\psi_{h,m}\rangle}{\langle\psi_{h,m}|\psi_{h,m}\rangle}+\frac{\langle\psi_{e,l}|H_e|\psi_{e,l}\rangle}{\langle\psi_{e,l}|\psi_{e,l}\rangle}+\frac{\langle\psi_{h,m}\psi_{e,l}|v|\psi_{e,l}\psi_{h,m}\rangle}{\langle\psi_{h,m}|\psi_{h,m}\rangle\langle\psi_{e,l}|\psi_{e,l}\rangle}=E^{m,l}, \tag{5}$$

where $E^{m,l}$ is the energy of the exciton corresponding to the electron in state l and the hole in state m.

The energy spectrum for a hole in a quantum dot is obtained by minimizing

$$\frac{\langle\psi_{h,m}|H_h|\psi_{h,m}\rangle}{\langle\psi_{h,m}|\psi_{h,m}\rangle}=E_h^m \tag{6}$$

for properly chosen basis functions for the hole. Here E_h^m is the energy for the mth energy state for the hole alone, not interacting with the electron. We note that estimates for energies of the excited states can be found by independent minimization with respect to the variational parameters.[39] For simplicity the indices m and l for the hole and electron states will be omitted below.

The exciton energies E are found iteratively by consecutive minimization of the hole and electron problem. This is done by solving the secular equations for an appropriate set of basis functions for the hole,

$$\frac{\langle\psi_h|H_h+V_{\rm eff}^e|\psi_h\rangle}{\langle\psi_h|\psi_h\rangle}=E_h, \tag{7}$$

where

$$V_{\rm eff}^e=V_{\rm eff}^e(\mathbf{r}_h)=\frac{\langle\psi_e^{n-1}|v|\psi_e^{n-1}\rangle}{\langle\psi_e^{n-1}|\psi_e^{n-1}\rangle} \tag{8}$$

with $|\psi_e^{n-1}\rangle$ fixed. [In the first step $(n=1)$ $V_{\rm eff}^e$ is omitted.] Thereafter we find the electron wave function by minimizing

$$\frac{\langle\psi_e^n|H_e+V_{\rm eff}^h|\psi_e^n\rangle}{\langle\psi_e^n|\psi_e^n\rangle}=E_e, \tag{9}$$

where

$$V_{\rm eff}^h=V_{\rm eff}^h(\mathbf{r}_e)=\frac{\langle\psi_h^n|v|\psi_h^n\rangle}{\langle\psi_h^n|\psi_h^n\rangle} \tag{10}$$

with $|\psi_h^n\rangle$ fixed. Here $V_{\rm eff}^e$ ($V_{\rm eff}^h$) is the Hartree potential felt by the electron (hole), while $|\psi_e^n\rangle$ ($|\psi_h^n\rangle$) is the electron (hole) wave function after the nth iteration. This alternating solution of the hole and electron problems is repeated until the values for E_h and E_e have converged. After convergence, the exciton binding energy E is given by

$$E=E_h+E_e-\frac{\langle\psi_h\psi_e|v|\psi_e\psi_h\rangle}{\langle\psi_h|\psi_h\rangle\langle\psi_e|\psi_e\rangle}. \tag{11}$$

The desired accuracy is typically reached after four or five iterations.

B. Electrons

In the single-band effective-mass theory the electron Hamiltonian H_e is given by

$$H_e=-\frac{\hbar^2}{2m_e}\nabla_e^2+V_{\rm QD}(\mathbf{r}_e), \tag{12}$$

where m_e is the spherical effective mass of the electron, and where

$$V_{\rm QD}(\mathbf{r}_e)=\begin{cases}0 & \text{for } |\mathbf{r}_e|<R\\ V_e & \text{for } |\mathbf{r}_e|\geq R\end{cases} \tag{13}$$

is the quantum dot potential.

In the experiments on excitons in CdSe quantum dots,[12] the CdSe dots were embedded in an optically transparent organic material [poly(vinyl butyral)]. The effective mass for this material is unknown, and we assume for simplicity the same effective mass in the surrounding material as inside the quantum dot. This should be unproblematic when the exciton is strongly confined to the quantum dot.

A Gaussian set is used as basis functions for the electron:

$$\psi_e^i(\mathbf{r}_e)=e^{-\beta_i r_e^2}. \tag{14}$$

The β's are chosen separately for each quantum dot state to minimize the energy of the state. A linear combination of seven $\psi_e^i(\mathbf{r}_e)$ with appropriately chosen β's is used in the calculations. These basis functions do not fulfill the infinite-offset ($V_e=\infty$) boundary conditions [$\psi_e(R)=0$], and for the description of the treatment for $V_e=\infty$ we refer to Ref. 29. Note that our choice of basis functions for the electrons makes it possible to study only electron states with spherical symmetry (denoted S_e). However, most of the exciton states identified in the experiments in Ref. 12 for CdSe dots are likely to correspond to S_e states, and we therefore limit ourselves to such states here.

The interaction between the electron and hole is assumed to be Coulombic:

$$v(|\mathbf{r}_e-\mathbf{r}_h|)=-\frac{e^2}{4\pi\epsilon|\mathbf{r}_e-\mathbf{r}_h|}. \tag{15}$$

Again for simplicity, the dielectric constant ϵ is taken as the bulk value of CdSe both in the dot and in the surrounding material. In Ref. 37 the incorporation of the Coulomb interaction in the calculational scheme is described in detail.

C. Holes

Because of the complexities of the valence-band structure, we use the effective bond-orbital model (EBOM) to describe the holes. Here we study quantum dots of hexagonal CdSe where a crystal-field term H_Δ splits the otherwise degenerate valence-band edge. Since the crystal-field splitting of the valence-band edges is relatively small in CdSe ($\approx$25 meV),[40] it has usually been neglected or treated as a perturbation in theoretical studies of quantum dots.[21,22]

We use two different types of EBOM hole descriptions. In the first description H_Δ is omitted. Then the system is cubic and corresponds to the point group T_d, and the hole basis functions used in the variational calculations are constructed

accordingly. Since the terms linear in **k** are neglected in the EBOM Hamiltonian, the correct point group for our model is O_h. However, in accordance with previous studies we will use the notation for the T_d group.[28]

In the other description the crystal-field term is included by adding to the Hamiltonian a diagonal term, which splits the otherwise fourfold degenerate band-edge states.[21,22,35] With this additional term the symmetry of the hole Hamiltonian corresponds to the symmetry of the EBOM Hamiltonian describing holes localized in quantum wells. We can therefore apply previously derived basis functions,[37,38] corresponding to systems with D_{2d} symmetry, in the present calculations incorporating the crystal-field term.

In Ref. 12 Norris *et al.* found that states with odd-parity envelopes for the hole play a minor part in explaining the experimental absorption spectra of CdSe quantum dots. In our present EBOM schemes for the hole (T_d and D_{2d}) we thus only consider hole states with even-parity envelopes.

Below we first describe the method used to investigate the cubic (T_d) system, and thereafter we present the basis set for the hexagonal (D_{2d}) system.

1. Treatment of cubic system

In T_d the electron spin ($s=1/2$) transforms as Γ_6, while the p-like valence orbitals transform according to the Γ_5 representation. Group theory gives $\Gamma_5\times\Gamma_6=\Gamma_7+\Gamma_8$. We want to incorporate both the heavy-hole, light-hole, and split-off valence bands in the calculations. Thus we include six spin-orbit-coupled bond orbitals (SOBOs), two Γ_7, and four Γ_8, to describe the hole:[28]

$$|\mathbf{R},u^{\Gamma_8}_{1/2}\rangle=-\frac{i}{\sqrt{2}}|\mathbf{R},x\rangle\phi^{\Gamma_6}_{-1/2}-\frac{1}{\sqrt{2}}|\mathbf{R},y\rangle\phi^{\Gamma_6}_{-1/2}, \quad (16)$$

$$|\mathbf{R},u^{\Gamma_8}_{-1/2}\rangle=\frac{i}{\sqrt{2}}|\mathbf{R},x\rangle\phi^{\Gamma_6}_{1/2}-\frac{1}{\sqrt{2}}|\mathbf{R},y\rangle\phi^{\Gamma_6}_{1/2}, \quad (17)$$

$$|\mathbf{R},u^{\Gamma_8}_{3/2}\rangle=\frac{i}{\sqrt{6}}|\mathbf{R},x\rangle\phi^{\Gamma_6}_{1/2}+\frac{1}{\sqrt{6}}|\mathbf{R},y\rangle\phi^{\Gamma_6}_{1/2}+i\frac{2}{\sqrt{6}}|\mathbf{R},z\rangle\phi^{\Gamma_6}_{-1/2}, \quad (18)$$

$$|\mathbf{R},u^{\Gamma_8}_{-3/2}\rangle=-\frac{i}{\sqrt{6}}|\mathbf{R},x\rangle\phi^{\Gamma_6}_{-1/2}+\frac{1}{\sqrt{6}}|\mathbf{R},y\rangle\phi^{\Gamma_6}_{-1/2}+i\frac{2}{\sqrt{6}}|\mathbf{R},z\rangle\phi^{\Gamma_6}_{1/2}, \quad (19)$$

$$|\mathbf{R},u^{\Gamma_7}_{1/2}\rangle=-\frac{i}{\sqrt{3}}|\mathbf{R},x\rangle\phi^{\Gamma_6}_{-1/2}+\frac{1}{\sqrt{3}}|\mathbf{R},y\rangle\phi^{\Gamma_6}_{-1/2}-\frac{i}{\sqrt{3}}|\mathbf{R},z\rangle\phi^{\Gamma_6}_{1/2}, \quad (20)$$

and

$$|\mathbf{R},u^{\Gamma_7}_{-1/2}\rangle=-\frac{i}{\sqrt{3}}|\mathbf{R},x\rangle\phi^{\Gamma_6}_{1/2}-\frac{1}{\sqrt{3}}|\mathbf{R},y\rangle\phi^{\Gamma_6}_{1/2}+\frac{i}{\sqrt{3}}|\mathbf{R},z\rangle\phi^{\Gamma_6}_{-1/2}. \quad (21)$$

Here **R** denotes a lattice site in the cubic lattice, $|\mathbf{R},\alpha\rangle$ denotes an α-like ($\alpha=x,y,z$) bond orbital at site **R**, and $\phi^{\Gamma_6}_{\pm 1/2}$ denotes the two electron spinors with spin directed in two opposite directions. We have used the Koster-Dimmock-Wheeler-Statz convention[41] (u^{Γ}_{ν}) for the SOBOs to derive Eqs. (16)–(21). The bond orbitals are assumed orthonormal, i.e., $\langle\mathbf{R},\alpha|\mathbf{R}',\alpha'\rangle=\delta_{\mathbf{R},\mathbf{R}'}\delta_{\alpha,\alpha'}$. The bond orbitals are also assumed sufficiently localized so that only nearest-neighbor interactions need to be included. The interaction matrix elements between the orbitals $|\mathbf{R},\alpha\rangle$ and $|\mathbf{R}',\alpha'\rangle$ for a fcc lattice are given by[27,42]

$$\langle\mathbf{R},\alpha|H|\mathbf{R}',\alpha'\rangle=E_p\delta_{\mathbf{R},\mathbf{R}'}\delta_{\alpha,\alpha'}+\sum_{\boldsymbol{\tau}}\delta_{\mathbf{R}-\mathbf{R}',\boldsymbol{\tau}}\{E_{xy}\boldsymbol{\tau}_\alpha\boldsymbol{\tau}_{\alpha'}(1-\delta_{\alpha,\alpha'})+[E_{xx}\tau^2_\alpha+E_{zz}(1-\tau^2_\alpha)]\delta_{\alpha,\alpha'}\}. \quad (22)$$

Here E_p is the interaction between bond orbitals at the same site, and $E_{\alpha,\alpha'}$ is the interaction between an α-like bond orbital located at the origin and an α'-like orbital located at $(1,1,0)a/2$, where a is the lattice constant of the cubic structure. The sum over $\boldsymbol{\tau}$ goes over the twelve nearest-neighbor position vectors in the fcc lattice.

The interaction parameters E_p, E_{xx}, E_{xy}, and E_{zz} are determined by expanding the tight-binding Hamiltonian, based on Eq. (22), to second order in **k** and requiring equivalence with multiband effective-mass theory.[27] In terms of the Luttinger parameters, the interaction parameters are found (in the hole picture[29]) to be given by the following expressions:

$$E_{xy}=-6\gamma_3\frac{\hbar^2}{2m_0a^2}, \quad E_{xx}=-(\gamma_1+4\gamma_2)\frac{\hbar^2}{2m_0a^2},$$
$$E_{zz}=-(\gamma_1-8\gamma_2)\frac{\hbar^2}{2m_0a^2}, \quad E_p=-E_v+12\gamma_1\frac{\hbar^2}{2m_0a^2}. \quad (23)$$

Here γ_1, γ_2, and γ_3 are the Luttinger parameters, m_0 is the rest mass of the electron, and E_v denotes the band edge of the heavy-hole and light-hole valence bands. Hole offsets are included in the model by choosing different E_v in the dot and barrier material. In the calculational scheme we assume that we have the same lattice structure on both sides of the quantum dot boundary. We also use the same material parameters in the barrier and dot materials. This is obviously not correct in our case,[12] but for states sufficiently localized to the dot, the error introduced should not be significant.

In principle, we could have used in a variational calculation a basis set consisting of six SOBOs per site in the cubic lattice. A large reduction of the basis set is, however, achieved by exploiting the symmetry of the system. We do this by expanding the hole wave function in exponential ra-

dial functions multiplied with symmetry-adapted angular basis functions. These symmetry-adapted basis functions are in turn combinations of products of cubic harmonics, ${}^{L}K_i^{\Gamma_\beta}$, multiplied with SOBOs.[28] The presuperscript L refers to the order of the cubic harmonic.[43]

We are interested in not only the Γ_8 ground state, but also in excited states, which have other symmetries as well (Γ_6 and Γ_7). However, the Γ_6 states are not optically active, and we will therefore focus only on the Γ_7 and Γ_8 states. The Γ_7 states are doubly degenerate ($\nu=1/2,-1/2$), and the Γ_8 states are fourfold degenerate ($\nu=3/2,1/2,-1/2,-3/2$). Hence it is only necessary to consider, say, the $\Gamma_8^{3/2}$ and $\Gamma_7^{1/2}$ states.

From Ref. 28 we have that the $\Gamma_8^{3/2}$ symmetry-adapted basis functions are given by ten different combinations of products of cubic harmonics and SOBOs; $|{}^{L}\psi_{3/2}^{\Gamma_8}(\mathbf{R})\rangle_a$, $|{}^{L}\psi_{3/2}^{\Gamma_8}(\mathbf{R})\rangle_b,\ldots,|{}^{L}\psi_{3/2}^{\Gamma_8}(\mathbf{R})\rangle_j$. The expressions for these $\Gamma_8^{3/2}$ basis functions and the corresponding five different $\Gamma_7^{1/2}$ basis functions can be found in Ref. 28, while the cubic harmonics can be found in Ref. 43.

In our calculations cubic harmonics corresponding to $L=0,\ 2,\ 4$, and 6 have been included, and this corresponds to a total of 28 angular basis functions for Γ_8 and 15 for Γ_7. In Sec. IVA and in the Appendix we will justify the neglection of cubic harmonics with $L\geqslant 8$. Note that with only even L's we restrict ourselves to states with even-parity envelopes. (To calculate states with odd-parity envelopes one would have to use a separate hole basis set including only cubic harmonics with odd L's.)

A spherical cluster with radius R_{clu} is used in the calculations, and we use the following basis functions for the Γ_8 and Γ_7 states:

$$|\psi_\mu^j\rangle_{n,m,L}=\sum_{\mathbf{R}}\ \cos\left(\frac{\pi}{2}\frac{\sqrt{x^2+y^2+z^2}}{R_{\mathrm{clu}}}\right)\times e^{-\alpha_n\sqrt{x^2+y^2+z^2}}|{}^{L}\psi_\mu^j(\mathbf{R})\rangle_m, \tag{24}$$

where $j,\ \mu=\Gamma_8,\ 3/2$ or $\Gamma_7,\ 1/2$. The subscripts $n,\ m$, and L refer to the radial basis function, the symmetry-adapted basis function ($a,b,\ldots,j$ for Γ_8 and $a,b,\ldots,e$ for Γ_7 in Ref. 28), and the order of the cubic harmonic, respectively. The basis functions are chosen to satisfy the zero-amplitude boundary condition at the cluster surface. The sum over $\mathbf{R}$ goes over all sites in the cluster, except (0,0,0). The largest cluster used in the calculations had a radius of 63 Å. The appropriate bond orbital at the center site is included separately in the basis.[29] Up to twelve appropriately chosen α's are used in the calculations. With up to 28 angular functions this gives a maximum of $12\times 28+1=337$ basis functions.

The quantum dot radius R is defined by[29]

$$R=\left(\frac{3N}{16\pi}\right)^{1/3}a, \tag{25}$$

where N is the number of sites in the quantum dot. In the infinite hole-offset case R_{clu} is equal to R.

2. Treatment of hexagonal system

For the hexagonal system we use basis functions with D_{2d} symmetry, and they are constructed in a similar way as the cubic T_d basis functions above. The D_{2d} EBOM basis functions have been used previously, and we refer to Refs. 29, 37, and 38 for a more thorough discussion.

In D_{2d} the electron spin ($s=1/2$) transforms as Γ_6, while the p-like valence orbitals transform according to the Γ_4 and Γ_5 representations. According to group theory $(\Gamma_4+\Gamma_5)\times\Gamma_6=\Gamma_6+\ {}^1\Gamma_7+\ {}^2\Gamma_7$. Thus in EBOM we describe the hole state by six spin-orbit-coupled bond orbitals (SOBOs), a Γ_6-like and two different Γ_7-like pairs: $|\mathbf{R},u_{1/2}^{\Gamma_6}\rangle=-|\mathbf{R},u_{1/2}^{\Gamma_8}\rangle$, $|\mathbf{R},u_{-1/2}^{\Gamma_6}\rangle=|\mathbf{R},u_{-1/2}^{\Gamma_8}\rangle$, $|\mathbf{R},{}^1u_{1/2}^{\Gamma_7}\rangle=|\mathbf{R},u_{-3/2}^{\Gamma_8}\rangle$, $|\mathbf{R},{}^1u_{-1/2}^{\Gamma_7}\rangle=|\mathbf{R},u_{3/2}^{\Gamma_8}\rangle$, $|\mathbf{R},{}^2u_{1/2}^{\Gamma_7}\rangle=|\mathbf{R},u_{1/2}^{\Gamma_7}\rangle$, and $|\mathbf{R},{}^2u_{-1/2}^{\Gamma_7}\rangle=|\mathbf{R},u_{-1/2}^{\Gamma_7}\rangle$, where the SOBOs for the hexagonal symmetry have been related to the cubic SOBOs in Eqs. (16)–(21).

The crystal-field splitting of the valence-band edges is included by adding the following on-site interaction:[22]

$$\langle\mathbf{R},u_\nu^\Gamma|H_\Delta|\mathbf{R}',u_{\nu'}^{\Gamma'}\rangle=-\delta_{\mathbf{R},\mathbf{R}'}\delta_{\nu\nu'}\delta_{\Gamma\Gamma'}\Delta(\Gamma), \tag{26}$$

where $\Delta(\Gamma)=\Delta$ for $\Gamma=\Gamma_6$, and $\Delta(\Gamma)=0$ for $\Gamma=\Gamma_7$. Here Δ is the value of the splitting between the A and B valence-band edges. We note in passing that holes in ellipsoidal quantum dots also can be approximately described by adding a term of the form given in Eq. (26) to the spherical dot Hamiltonian.[36,44] The results presented for hole energies for Δ in the range 0–100 meV can thus also be applied to ellipsoidal quantum dots.

As for the cubic case, the hole wave function is expanded in a set of symmetry-adapted angular functions multiplied with exponential radial functions.[29,37] We need separate basis function sets for the Γ_6 and Γ_7 hole states. For example, the Γ_6 basis functions are given by nine different combinations of products of angular functions and SOBOs: $|\psi_{1/2}^{\Gamma_6}(\mathbf{R})\rangle_a$, $|\psi_{1/2}^{\Gamma_6}(\mathbf{R})\rangle_b,\ldots,|\psi_{1/2}^{\Gamma_6}(\mathbf{R})\rangle_i$. They are listed in Ref. 29. The angular functions for the Γ_7 case are given accordingly.[37] Note that these angular basis functions correspond to cubic harmonics with $L=0$ and 2 only.

This gives the following basis functions:

$$|\psi_{1/2}^{\Gamma_{6,7}}\rangle_{n,m}=\sum_{\mathbf{R}}\ \cos\left(\frac{\pi}{2}\frac{\sqrt{x^2+y^2+z^2}}{R_{\mathrm{clu}}}\right)\times e^{-\alpha_n\sqrt{x^2+y^2+\mu_n z^2}}|\psi_{1/2}^{\Gamma_{6,7}}(\mathbf{R})\rangle_m, \tag{27}$$

where m refers to one of the nine angular functions. We have introduced anisotropy parameters μ_n in the exponentials to allow for more flexibility in the wave function. However, for most optically important states the isotropic choice $\mu_n=1$ was found to be favorable. We have used up to twelve different α's (and μ's) in our computations which together with the appropriate SOBO on the central-cell site give a total of $(12\times 9)+1=109$ basis functions.

D. Oscillator strengths

In this subsection we derive expressions for the oscillator strength for localized excitons in the cubic system. For the

corresponding expressions for the oscillator strength in the hexagonal system where D_{2d} basis functions are used, we refer to Ref. 37.

Within the effective-mass formalism the oscillator strength f for the bound exciton has the form[45,46]

$$f_i=\frac{2}{m_0E_0}\sum_j |\langle u_{c0}|p_i|u_{v0}^j\rangle|^2\left|\int d^3r \quad \psi_e(\mathbf{r})\psi_h^j(\mathbf{r})\right|^2, \tag{28}$$

when a separable wave function for the exciton, i.e.,

$$\Psi(\mathbf{r}_e,\mathbf{r}_h)=\left(\sum_j \psi_h^j(\mathbf{r}_h)u_{v0}^j(\mathbf{r}_h)\right)\psi_e(\mathbf{r}_e)u_{c0}(\mathbf{r}_e), \tag{29}$$

is assumed. The subscript i in Eq. (28) denotes the polarization direction of the light, E_0 is the energy of the transition, u_{c0} is the Γ-point conduction-band Bloch function in bulk, u_{v0}^j denotes the Γ-point valence-band Bloch function with the same symmetry as the SOBO $|\mathbf{R},u_{m_j}^{\Gamma_j}\rangle$, and ψ_e and ψ_h^j are envelope functions for the electron and hole, respectively. Since we use the EBOM to describe the holes, Eq. (28) must be modified correspondingly. In Ref. 37 the analog expression

$$f_i=\frac{2}{m_0E_0}\sum_j |\langle u_{c0}|p_i|u_{v0}^j\rangle|^2V_\Omega\left|\sum_{\mathbf{R}} G_j(\mathbf{R})\psi_e(\mathbf{R})\right|^2 \tag{30}$$

for the oscillator strength for a bound exciton has been derived. Here $G_j(\mathbf{R})$ is related to the EBOM hole wave function $|\psi_h\rangle$ via

$$|\psi_h\rangle=\sum_{\mathbf{R},j} G_j(\mathbf{R})|\mathbf{R},u_{m_j}^{\Gamma_j}\rangle, \tag{31}$$

and V_Ω denotes the volume of the primitive cell.

In our calculations the symmetry of the electron wave function ψ_e is spherical. For cubic symmetry only the hole basis functions consisting of angular symmetry-adapted functions with Γ_1 symmetry may give nonzero contributions in Eq. (30). This is because only these basis functions belong to the same irreducible representation as the spherically symmetric electron wave function. Thus only a small subset of the hole basis functions will contribute in Eq. (30),[37] and the expression for the oscillator strength for a j-like bound exciton simplifies to

$$f_i=\frac{2}{m_0E_0}|\langle u_{c0}|p_i|u_{v0}^j\rangle|^2V_\Omega\left|\sum_{\mathbf{R}} G_j(\mathbf{R})\psi_e(\mathbf{R})\right|^2. \tag{32}$$

From Eq. (32) we observe that the oscillator strength is given by the overlap factor

$$K=V_\Omega\left|\sum_{\mathbf{R}} G_j(\mathbf{R})\psi_e(\mathbf{R})\right|^2 \tag{33}$$

multiplied by a prefactor. The overlap factor K depends only on the envelopes of the exciton wave function and is the same for all the degenerate Γ_8 states. In contrast, the prefactor is different for the $\Gamma_8^{\pm 3/2}$ and $\Gamma_8^{\pm 1/2}$ states and depends also on the direction of polarization. In this paper we present only overlap factors (for normalized wave functions) which easily can be combined with the appropriate prefactor to determine desired oscillator strengths.

TABLE I. Material parameters for CdSe.

Parameter	Parameter values (CdSe)
Dielectric constant $\epsilon(0)$	$9.2\epsilon_0$
Band gap E_g	1840 meV
Lattice constant a	6.052 Å
Electron effective mass m_e	$0.13m_0$
Electron offset V_e	600 meV, ∞
Spin-orbit splitting λ	420 meV
Hole offset V_h	600 meV, 1000 meV, ∞
First Luttinger set	$\gamma_1=1.66,\ \gamma_2=\gamma_3=0.41$
Second Luttinger set	$\gamma_1=1.66,\ \gamma_2=0.41,\ \gamma_3=0.53$
Third Luttinger set	$\gamma_1=1.66,\ \gamma_2=0.347,\ \gamma_3=0.452$
Crystal-field splitting Δ	25 meV

III. CHOICE OF MATERIAL PARAMETERS

In this section we discuss our choice of material parameters for CdSe used in the calculations. In Table I these parameters are summarized. The values for the electron effective mass $m_e=0.13m_0$, the cubic lattice constant $a=6.052$ Å, the spin-orbit splitting $\lambda=420$ meV, and the crystal-field splitting $\Delta=25$ meV have been taken from Landolt-Börnstein.[40] We have used the low temperature (100 K) static dielectric constant $\epsilon(0)=9.2\epsilon_0$, where ϵ_0 is the vacuum permittivity. This is an average of the dielectric constants[40] $\epsilon_\perp(0)=9.15\epsilon_0$ and $\epsilon_\parallel(0)=9.29\epsilon_0$. The subscripts $\parallel$ and $\perp$ denote parallel and perpendicular to the hexagonal axis, respectively. Since there is some controversy whether to choose the static dielectric constant $\epsilon(0)$ or the optical dielectric constant $\epsilon(\infty)$,[1,47] we will also discuss the consequences of alternative choices for the dielectric constant.

Ekimov *et al.*[11] used the Luttinger parameter set $\gamma_1=2.1,\ \gamma_2=\gamma_3=0.55$ for CdSe. This Luttinger parameter set was adapted to experimental results on CdSe quantum dots. We will, however, adapt our Luttinger parameters to experimental values of bulk CdSe effective masses.

For hexagonal bulk CdSe the effective masses corresponding to the two upper valence bands, which are split by the crystal field Δ, are traditionally denoted by subscripts A and B. Effective hole masses parallel and perpendicular to the hexagonal axis are denoted by the subscripts $\parallel$ and $\perp$, respectively. The Luttinger parameters are connected to the effective hole masses $m_{\parallel A}$, $m_{\perp A}$, $m_{\parallel B}$, and $m_{\perp B}$ for bulk CdSe in the hexagonal phase by[21,48] $m_{\parallel A}=m_0/(\gamma_1-2\gamma_2)$, $m_{\perp A}=m_0/(\gamma_1+\gamma_2)$, $m_{\parallel B}=m_0/(\gamma_1+2\gamma_2)$, and $m_{\perp B}=m_0/(\gamma_1-\gamma_2)$. From Landolt-Börnstein[40] we find the following experimental values for the hole masses: $m_{\parallel A}=1.17m_0$, $m_{\perp A}=0.375m_0$, and $m_{\perp B}=0.92m_0$.[49] To our knowledge there are no experimental values for $m_{\parallel B}$.

Our first set of Luttinger parameters, $\gamma_1=1.66,\ \gamma_2=\gamma_3=0.41$, is found by minimizing $(m_{\parallel A,t}-m_{\parallel A,\text{expt.}})^2+(m_{\perp A,t}-m_{\perp A,\text{expt.}})^2+(m_{\perp B,t}-m_{\perp B,\text{expt.}})^2$ with respect to the Luttinger parameters, assuming $\gamma_2=\gamma_3$ and using the formulas given above for the connections between the Lut-

tinger parameters and the effective hole masses. Here the subscript t (expt.) on the effective masses denotes theoretical (experimental) values. The resulting theoretical effective hole masses ($m_{\parallel A,t}=1.19m_0, m_{\perp A,t}=0.48m_0$, $m_{\perp B,t}=0.80m_0$, and $m_{\parallel B,t}=0.40m_0$) are in good agreement with the corresponding experimental values for hexagonal CdSe.

Note, however, that by choosing these Luttinger parameters with $\gamma_2=\gamma_3$, we have neglected the nonspherical terms in the Luttinger Hamiltonian.[32] To our knowledge the ratio between γ_2 and γ_3 is not known for CdSe. Using the Luttinger parameters listed in Lawaetz,[50] we observe that the ratio between γ_2 and γ_3 is quite similar for ZnSe ($\gamma_2=1.24$, $\gamma_3=1.67$) and ZnTe ($\gamma_2=1.07$, $\gamma_3=1.64$). Assuming that the ratio between γ_2 and γ_3 is the same for CdSe and CdTe ($\gamma_2=1.89$, $\gamma_3=2.46$),[50] we obtain the second set of Luttinger parameters $\gamma_1=1.66$, $\gamma_2=0.41$, $\gamma_3=0.53$ for CdSe. With this Luttinger parameter set there will be cubic terms in the Hamiltonian.[17,18] For reasons explained in the next section we will also use the third Luttinger parameter set in Table I.

The band-gap energy E_g is not a parameter in our EBOM calculations, but in order to compare EBOM results with experiments, we need this parameter. From Landolt-Börnstein[40] we have $E_g=1.84$ eV for hexagonal CdSe.

CdSe quantum dots can be embedded in different types of materials and the values of the electron offset V_e and the hole offset V_h for these structures are generally not known. Several values of the electron and hole offsets are therefore used in the calculations.

IV. HOLE ENERGIES

A. Comparison of EBOM and SMEMT

In the following the EBOM hole energy spectra are compared with the corresponding hole spectra obtained using the SMEMT. The SMEMT used earlier by Ekimov *et al.*[11] for CdSe quantum dots includes both the heavy-hole, the light-hole, and the split-off valence bands, and the hole offset is assumed infinite. With SMEMT the hole energies can be found from numerical root-finding of transcendental equations, and this method thus requires less work than the EBOM. Therefore it is important to compare the results obtained by these methods to investigate when the simpler SMEMT method is sufficient and when the more extensive EBOM calculational scheme must be used. For the lowest-lying hole energies such a comparison has previously been done for CdSe (Ref. 31) and GaAs.[51]

With the spherically symmetric Hamiltonian inherent in the SMEMT the total angular momentum F and the parity are good quantum numbers. We recall that $\mathbf{F}=\mathbf{L}+\mathbf{J}$, where $\mathbf{L}$ is the orbital angular momentum operator for the envelope wave function, and $\mathbf{J}$ represents the spin operator. We use the common notation n_hQ_F ($Q=S,P,D,F,G,\ldots$) where the states are labeled by the smallest angular momentum L in the envelope, and n_h is the number of the level with a certain symmetry.[11] Each hole state has contributions only from L and $L+2$ in the spherical approximation. The cubic lattice structure of CdSe will split some of the energy levels that are degenerate in the spherically symmetric system. In Table II we have shown the compatibility table between the representations with spherical and cubic T_d symmetry.[41] This table shows how energy levels which are degenerate in a spherically symmetric system are split by the cubic lattice structure.

TABLE II. Compatibility between spherical symmetry [the full rotational group $O(3)$] and cubic symmetry (the T_d point group) for states with even-parity envelopes.

Spherical symmetry $[O(3)]$	Cubic symmetry (T_d)
$S_{1/2}$	Γ_7
$S_{3/2}$	Γ_8
$D_{5/2}$	$\Gamma_6+\Gamma_8$
$D_{7/2}$	$\Gamma_6+\Gamma_7+\Gamma_8$
$G_{9/2}$	$\Gamma_7+2\Gamma_8$

Cubic harmonics corresponding to $L=0$, 2, 4, and 6 have been included in the EBOM hole basis functions. In the SMEMT this suffices to describe the S, D, and G states since these states have contributions only from $L=0$ and 2, $L=2$ and 4, and $L=4$ and 6, respectively.[11] The lowest-lying hole states generally correspond to small angular momenta, and an accurate description of the S, D, and G states is sufficient for the present purpose. In the Appendix this is demonstrated more clearly by showing the relative importance of contributions from different L's for the ten lowest Γ_8 and five lowest Γ_7 states.

In Fig. 1 the energy spectrum for low-lying hole states in CdSe is shown as a function of the dot radius for an infinite hole offset for the cubic EBOM and the SMEMT using identical material parameters. The SMEMT results are found from the transcendental equations used in Ref. 11.

From Table II and Fig. 1 we see that the $1S_{3/2}$ state corresponds to the lowest Γ_8 state ($1\Gamma_8$) and that the $1D_{5/2}$ state should generate both a Γ_8 and a Γ_6 state in the cubic case. The SMEMT curves for $2S_{3/2}$ and $1D_{5/2}$ are seen to intersect at $R\approx 18$ Å. In the EBOM model this gives rise to an avoided crossing between $2\Gamma_8$ and $3\Gamma_8$. Note that we have not included Γ_6 states because only states corresponding to the $S_{1/2}$ and $S_{3/2}$ states (Γ_7 and Γ_8) will be optically active. This negligible oscillator strength for the cubic Γ_6 states was also verified directly for some Γ_6 exciton states using our hexagonal EBOM program.

According to Table II the $1D_{7/2}$ state should give rise to a Γ_8, a Γ_7, and a Γ_6 state. For large radii ($R\sim 30-50$ Å) the $1D_{7/2}$ state is seen to correspond to $4\Gamma_8$ and $1\Gamma_7$, which are nearly degenerate. The reason why the $4\Gamma_8$ and $1\Gamma_7$ states are not completely degenerate even with $\gamma_2=\gamma_3$ is presumably the cubic lattice inherent in the EBOM method. The influence of the cubic lattice is, however, less for large dot radii than for small dot radii as expected.

For small dot radii ($R<20-30$ Å) the SMEMT gives considerably larger hole energies than the EBOM. This is in qualitative agreement with previous comparisons between EBOM and effective-mass theories.[29] For the largest dot radii ($R>40-50$ Å) the differences between the two models are small, at least for the lowest states.

In Fig. 2 we show the cubic EBOM hole spectra for finite offsets (1000 meV and 600 meV), which will be needed when calculating exciton *binding* energies in Sec. V C. As

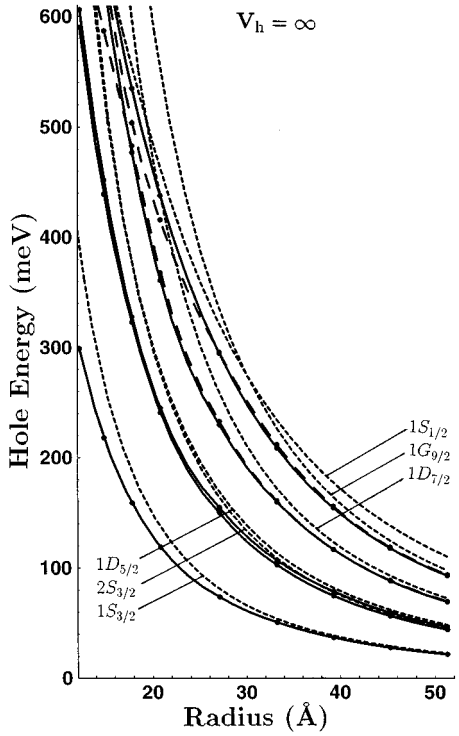

FIG. 1. Hole energies E_h for several states as functions of the dot radius R for infinite hole offset for the cubic EBOM ($\Delta=0$) and SMEMT methods. The material parameters for CdSe in Table I with $\gamma_1=1.66$, $\gamma_2=\gamma_3=0.41$ have been used. The five solid curves correspond to interpolations of numerical EBOM results (marked as dots) for the five lowest Γ_8 states, and correspondingly the two long-dashed curves give the two lowest Γ_7 states. The six dotted curves show the SMEMT results for the $1S_{3/2}$, $2S_{3/2}$, $1D_{5/2}$, $1D_{7/2}$, $1G_{9/2}$, and $1S_{1/2}$ states which are the six lowest hole states with even-parity envelopes for large radii.

expected, lower offsets result in lower energies due to reduced confinement of the hole.

We also tested EBOM for the lowest energy states against the finite-offset SMEMT scheme used by Sercel and Vahala,[20] who did not include the spin-orbit split-off band. The comparison, not shown here, shows the same good agreement for large radii as for the infinite-offset case.

In Fig. 3 we show the hole spectra for $\gamma_1=1.66$, $\gamma_2=0.41$, $\gamma_3=0.53$, and $V_h=\infty$. The only difference between the material parameters used in Fig. 1 and Fig. 3 is the value of γ_3. By comparing the cubic EBOM states in Fig. 1 and Fig. 3 carefully, we see that the hole states with $\gamma_3=0.53$ have somewhat lower energies than the corresponding states for $\gamma_3=0.41$. For the ground-state energy $1\Gamma_8$ we find the maximal difference between the two Luttinger parameter sets for dot radii in the range 12 Å–51 Å to be 14 meV. For the five lowest Γ_8 states we find the largest difference to be 115 meV, and for the two lowest Γ_7 states we find 100 meV. Generally, for both the Γ_7 and Γ_8 states, we find the largest differences in the hole energies for small dot radii and for the higher-lying states.

We have also done calculations for finite offset, $V_h=1000$ meV, with $\gamma_1=1.66$, $\gamma_2=0.41$, $\gamma_3=0.53$. The results lead to the same qualitative conclusions as for infinite offset.

By increasing γ_3 from 0.41 to 0.53, we not only include cubic terms in the Hamiltonian, we also change the spherical terms.[17,18,52] In order to do a more transparent investigation of the influence of cubic terms, we have done calculations for the Luttinger parameter set $\gamma_1=1.66$, $\gamma_2=0.347$, $\gamma_3=0.452$. With this parameter set cubic terms are introduced in the Hamiltonian without changing the spherical terms compared to the parameter set $\gamma_1=1.66$, $\gamma_2=\gamma_3=0.41$. For infinite hole offset we find that the maximal change from the cubic terms to the ground-state hole energy for dot radii in the range 12 Å–51 Å is less than 3 meV. For the five lowest Γ_8 states we find the largest difference to be 17 meV, and for the two lowest Γ_7 states we find, correspondingly, 37 meV. The largest deviation between the hole energies of the two Luttinger parameter sets is found for small dot radii. However, we may conclude that inclusion of cubic terms in the Hamiltonian has little effect on the energies of the lowest hole states.

Figure 4 exhibits the hole energy spectra as functions of the spin-orbit energy λ for a fixed radius ($R=20.8$ Å) using the cubic EBOM and the SMEMT with infinite offsets. The cubic Γ_6 states are not included. As observed in Fig. 1, several crossings of energy states in the SMEMT [Fig. 4(b)] are seen to correspond to avoided crossings in the EBOM results [Fig. 4(a)]. The crossing of, e.g., the $1D_{5/2}$ and the $2S_{3/2}$ state for $\lambda\approx 300$ meV can be seen as an avoided crossing between the $2\Gamma_8$ and $3\Gamma_8$ states. Apart from this, the qualitative features are the same. As in Fig. 1, the EBOM hole states are observed to have smaller energies than the corresponding SMEMT states. The largest difference is observed for the higher hole states. From Fig. 4 we can also see that for this dot radius the decoupling of the spin-orbit split-off band (i.e., $\lambda=\infty$) is a good approximation for CdSe (with $\lambda=420$ meV) for the four lowest Γ_8 states. However, for the Γ_7 states (except $1\Gamma_7$) this approximation cannot be used since these states have major contributions from the split-off band.

We may conclude that the SMEMT and EBOM give qualitatively similar hole energy spectra. For large radii the two methods also give quantitatively similar results, while for small dot radii the SMEMT gives larger hole energies than the EBOM. This is reasonable since the EBOM dispersion relation, fitted to agree with the SMEMT dispersion relation close to the zone center, is predominantly lower (in the hole picture) than the SMEMT dispersion relation for large wave vectors.[27]

B. Crystal-field term

In this subsection the crystal-field term in the hole Hamiltonian due to the hexagonal structure of CdSe will be included in the calculations. The crystal-field term splits the fourfold degenerate Γ_8 states in the cubic system into two pairs of doubly degenerate states denoted Γ_6^D and Γ_7^D. To avoid confusion we have added the superscript D to denote that the D_{2d} (and not the T_d) notation is used.

Efros[21] has derived expressions for the splitting of the $1\Gamma_8$ states as a function of the crystal-field splitting Δ in the SMEMT approximation. In Efros' work, Δ was treated as a perturbation. Some manipulations of Efros' results give

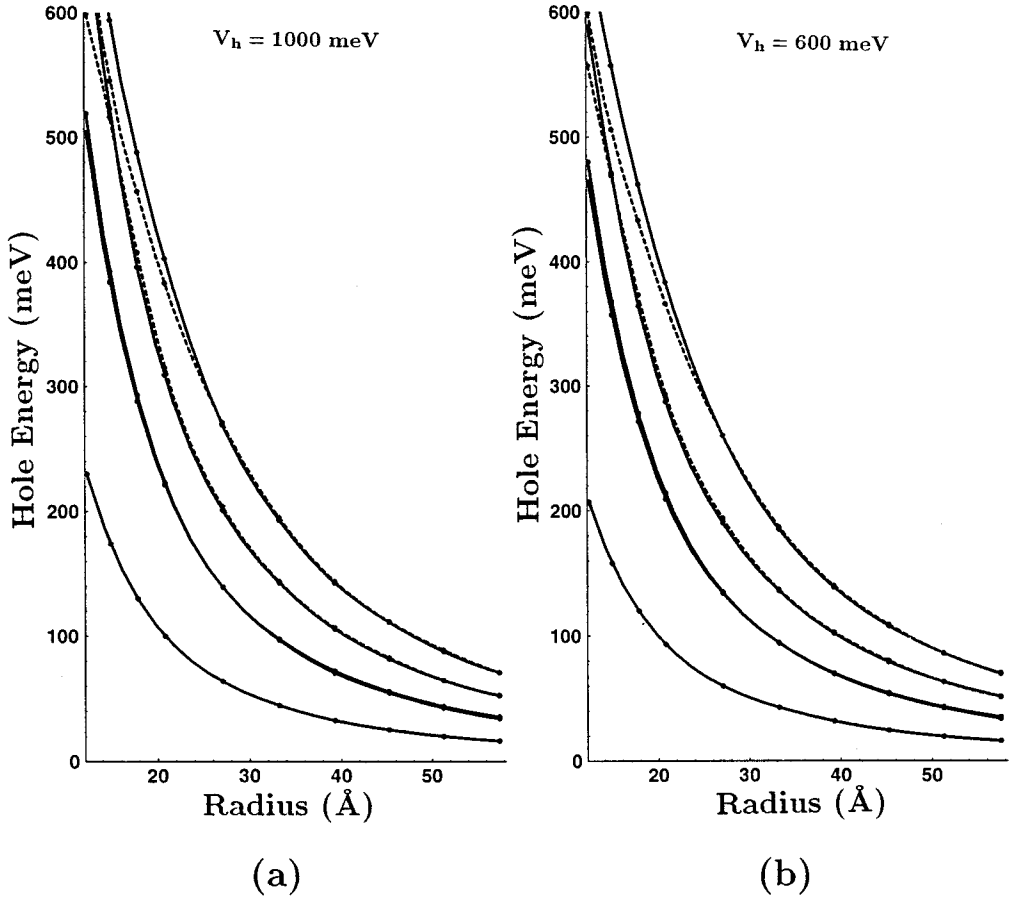

FIG. 2. (a) Hole energies E_h for several different states as functions of the dot radius R for a hole offset $V_h=1000$ meV calculated with the cubic EBOM ($\Delta=0$). Except for the hole offset the same material parameters as in Fig. 1 have been used. The five solid curves are interpolations of numerical results (marked as dots) for the five lowest Γ_8 states, and correspondingly the two dotted curves show the two lowest Γ_7 states. (b) Same as for (a), but $V_h=600$ meV.

$$\delta_{1\Gamma_6^D}=-\frac{1}{2}\Delta[1+v(\beta)], \quad \delta_{1\Gamma_7^D}=-\frac{1}{2}\Delta[1-v(\beta)]. \tag{34}$$

Here $\delta_{1\Gamma_6^D}$ and $\delta_{1\Gamma_7^D}$ denote the splitting in energy $[\delta=E_h(\Delta)-E_h(\Delta=0)]$ between the cubic $1\Gamma_8$ states and the $1\Gamma_6^D$ and $1\Gamma_7^D$ states, respectively, and $\beta=m_{\|B}/m_{\|A}$. Numerical values of the function $v(\beta)$ are found in Efros' article.[21]

In EBOM the crystal-field term is included by adding the on-site interaction term given in Eq. (26) to the Hamiltonian. We could have studied the effect of Δ perturbatively using the cubic EBOM program. However, by using our hexagonal EBOM program with D_{2d} basis functions, we can do a full nonperturbative calculation.

In Fig. 5 the splittings of the EBOM hole energies for the $1\Gamma_8$ and $2\Gamma_8$ cubic states into $1\Gamma_6^D$, $1\Gamma_7^D$ and $2\Gamma_6^D$, $2\Gamma_7^D$ states, respectively, due to the crystal-field term are shown as functions of the crystal-field splitting Δ for the dot radii $R=20.8$ Å and $R=51.3$ Å. Figure 5(a) shows that for $R=20.8$ Å the agreement between the hexagonal EBOM results and the perturbative SMEMT results [Eq. (34)] is generally good for both the $1\Gamma_6^D$ and $1\Gamma_7^D$ states. Figure 5(a) further shows that the splitting between the $2\Gamma_6^D$ and $2\Gamma_7^D$ states due to the crystal-field term is less than the splitting between the $1\Gamma_6^D$ and $1\Gamma_7^D$ states.

The results for $R=51.3$ Å are shown in Fig. 5(b). We see that increasing R has a negligible influence on the effect of the crystal-field term on the energy of the $1\Gamma_6^D$ state. However, the $1\Gamma_7^D$ is affected, and the deviation between EBOM and SMEMT results is seen to be substantial for $\Delta>30-40$ meV. The reason for the qualitative difference between the results for $R=20.8$ Å and $R=51.3$ Å is presumably that the perturbative Efros formulas are only applicable as long as Δ is much less than typical hole confinement energies, which are roughly proportional to R^{-2}.

Also for $R=51.3$ Å we observe that the splitting between the $2\Gamma_6^D$ and $2\Gamma_7^D$ states from the crystal-field term is less than the splitting between the $1\Gamma_6^D$ and $1\Gamma_7^D$ states.

In conclusion, since the crystal-field splitting is ≈ 25 meV for CdSe, our EBOM results indicate that Efros' formulas, Eq. (34), can be applied for the splitting of the ground state, at least for dots with radii <50 Å.

V. EXCITON ENERGIES

This section is divided into five parts. In the first subsection the exciton ground-state energy is calculated and com-

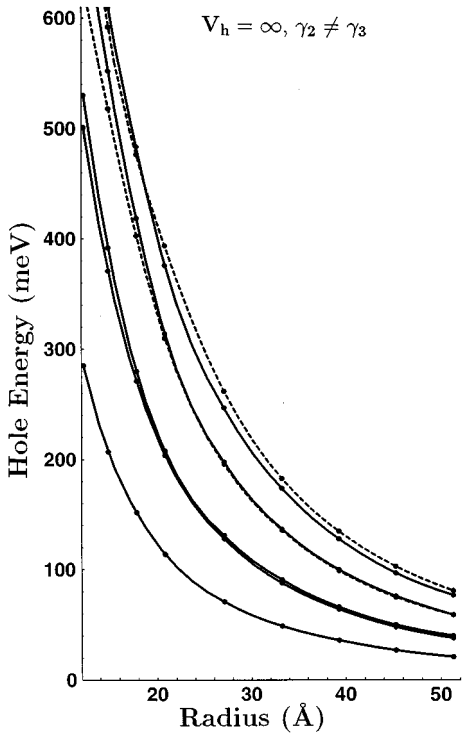

FIG. 3. Same as in Fig. 2, but with infinite hole offset ($V_h=\infty$) and $\gamma_1=1.66$, $\gamma_2=0.41$, and $\gamma_3=0.53$.

pared with numerous experimental results. The second subsection contains results for the exciton energy spectra and oscillator strengths. The results are compared both with recent experiments[12] and with SMEMT results. The binding energies of different exciton states are presented in the third subsection. In the fourth subsection the influence of the crystal-field splitting term on exciton energies and oscillator strengths is studied. Finally, in the last subsection we discuss the effect of other choices of dielectric constants.

A. Exciton ground state

In Fig. 6 we compare results for CdSe exciton ground-state energies based on our combined cubic EBOM-EMT scheme [cubic EBOM for the hole, single-band effective-mass theory (EMT) for the electron] with various experimental results for CdSe quantum dots. In Fig. 6(a) we have compared the EBOM-EMT results with the experimental results of Norris *et al.*[12] In Fig. 6(b) the same EBOM-EMT results are compared with other experiments[3–6,8,9,11] for the exciton ground state. We have used the Luttinger parameters $\gamma_1=1.66$, $\gamma_2=\gamma_3=0.41$, while the other material parameters are listed in Table I.

While the band gap E_g of CdSe is known to be close to 1.84 eV,[40] the electron and hole offsets are generally unknown. For instance, E_g of optically clear poly(vinyl butyral) is not known. However, if the material does not absorb visible light, we can estimate that $E_g>3$ eV. For the case with equal electron and hole offsets, we thus estimate $V_e, V_h \geqslant 0.6$ eV.

In Fig. 6 we show cubic EBOM-EMT exciton energies for several choices of offsets ($V_h=V_e=\infty$, $V_h=V_e=1000$ meV, $V_h=V_e=600$ meV, and $V_h=\infty, V_e=600$ meV). We see from Fig. 6(a) that the infinite-offset EBOM-EMT calculations overestimate the ground-state energy compared to the experiments of Norris *et al.*[12] We also see from Fig. 6 that for the infinite-offset case the EBOM-EMT scheme gives slightly lower ground-state energies than the combined SMEMT-EMT scheme with the Coulomb interaction included perturbatively. The finite-offset results, particularly the case with $V_h=V_e=600$ meV, are seen to fit these experiments well, however. For the more scattered experimental results shown in Fig. 6(b) the situation is less clear, but also here the infinite-offset results seem to overestimate most of the experimental results. Note, however, that the experiments shown in Fig. 6(b) correspond to CdSe quantum dots in various matrix materials, and the offsets will thus not be the same for all experimental points shown. Note also that the ground-state energies are much more susceptible to the electron offset than the hole offset. This is illustrated in Fig. 6 by the relatively small difference between the EBOM-EMT results for $V_h=\infty$ and $V_h=600$ meV with finite electron offset ($V_e=600$ meV).

We have also performed EBOM-EMT calculations for the ground-state exciton energy with $\gamma_1=1.66$, $\gamma_2=0.41$, and $\gamma_3=0.53$ with the other material parameters the same as in Fig. 6. Both for infinite offsets ($V_e=V_h=\infty$) and for finite offsets ($V_e=V_h=1000$ meV), we find that increasing γ_3 from 0.41 to 0.53 lowers the ground-state energy with less than 15 meV for dot radii in the range 15 Å–51 Å. The difference in the ground-state exciton energy between the two choices of Luttinger parameters is largest for small dot radii. The main conclusion is, however, that the results for the ground-state exciton energy are quite similar for the two Luttinger parameter sets.

Calculations based on tight-binding methods[23,24] and pseudopotential methods,[25,26] which for numerical capacity reasons so far have been limited to the infinite-offset case, predict lower confinement energies than EBOM and effective-mass theories.[29] Since EBOM is fitted to give the correct bulk band structure for small wave vectors and predicts too wide hole bands,[27] it is to be expected that EBOM, as well as effective-mass theories, overestimate confinement energies for small dot radii. However, the error involved in using EMT for the electron and EBOM for the hole is expected to be reduced for smaller offsets when penetration of the wave functions into the barrier matrix becomes significant.

B. Exciton spectra and oscillator strengths

In Figs. 7–10 we present results for CdSe exciton energies and overlap factors based on our combined cubic EBOM-EMT scheme for comparison with the experimental exciton spectra from Norris *et al.*[12] We use the notation $n_h\Gamma_{8,7}-n_eS_e$ appropriate for cubic hole symmetry. Many of the lowest exciton states have a negligible oscillator strength and are not expected to be seen experimentally. In order to compare with the experiments we have thus marked the states in the figures according to the magnitude of their overlap factor K. As seen in the previous subsection the exciton ground-state energy depends sensitively on the electron off-

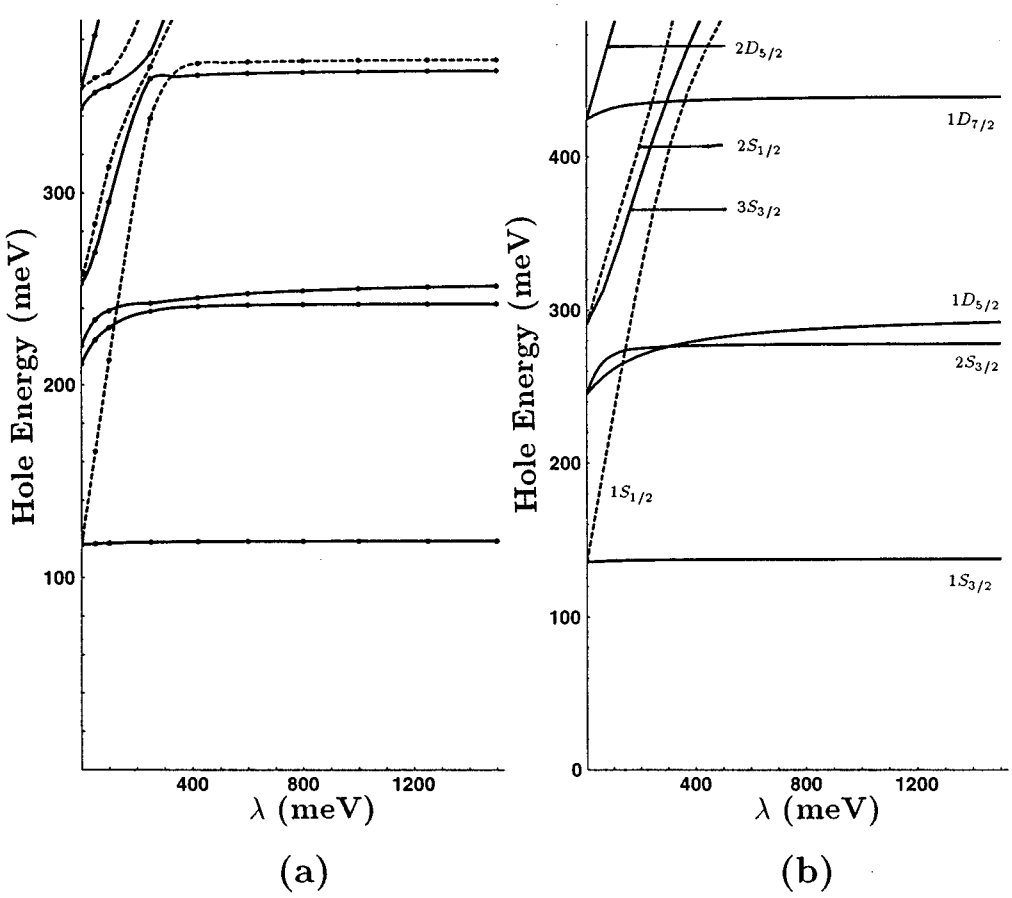

FIG. 4. Cubic EBOM ($\Delta=0$) and SMEMT hole energies for several states as functions of the spin-orbit splitting λ for a fixed dot radius $R=20.8$ Å. The results of the six lowest Γ_8 states (solid curves) and the three lowest Γ_7 states (dotted curves) calculated with the EBOM are drawn in (a). The curves are found by interpolations of the numerical results marked as dots. The parameters used are $\gamma_1=1.66$, $\gamma_2=\gamma_3=0.41$, and $V_h=\infty$. The corresponding SMEMT states are shown in (b). Note that to facilitate easy comparison the energy scales are different in the two figures.

set. Since most of the experimentally observed transitions involve the same electron level ($1S_e$),[12] we have plotted the transition energies relative to the exciton ground-state energy ($1\Gamma_8-1S_e$) because this energy is measured experimentally more precisely than the dot size,[12] and because this reduces the sensitivity to the choice of electron offset in our model.

In Table III we list the overlap factor K for the $n_h\Gamma_{7,8}-1S_e$ exciton states in the infinite-offset case for a set of dot radii. For the Γ_8-1S_e states most of the oscillator strength is seen to be distributed between the $1\Gamma_8-1S_e$ and $2\Gamma_8-1S_e$ states, with only minor contributions from the $3\Gamma_8-1S_e$ and higher-lying states. For the $n_h\Gamma_7-1S_e$ states the situation is more complicated, and for large dots the states with large oscillator strengths are seen to correspond to large values of n_h ($n_h=23$ for $R=51.3$ Å). This feature is explained below.

In Fig. 7(a) our cubic EBOM-EMT results for infinite hole and electron offsets are compared with the experiments. As seen in Table III, only the three lowest Γ_8-1S_e states ($1\Gamma_8-1S_e$, $2\Gamma_8-1S_e$, $3\Gamma_8-1S_e$) have values for the overlap factor larger than 0.01 in the infinite-offset case. Therefore only results for the $2\Gamma_8-1S_e$ and $3\Gamma_8-1S_e$ transitions are shown in Fig. 7(a). For the Γ_7-1S_e states the overlap factor depends sensitively on the quantum dot radius R. In Fig. 7(a) it is seen that many of the Γ_7-1S_e transitions with a large overlap factor are lifted by approximately the spin-orbit energy $\lambda=420$ meV compared to the $1\Gamma_8-1S_e$ transition.

In Fig. 7(b) we compare theoretical exciton energies using SMEMT for the hole and EMT for the electron with the same experiments as in Fig. 7(a). The Coulomb interaction is treated as a perturbation.[11] For transitions to S_e states we use the Efros estimate $V_{eh}=1.8e^2/(4\pi\epsilon R)$, and for transitions to the $1P_e$ level we use $V_{eh}=1.7e^2/(4\pi\epsilon R)$.[53,54] A collection of low-lying exciton states, both even-parity and odd-parity, which were found to have significant oscillator strengths in Ref. 11, are shown.

From Figs. 7(a) and 7(b) we see that both the infinite-offset cubic EBOM-EMT results for the $2\Gamma_8-1S_e$ and $3\Gamma_8-1S_e$ states and the infinite-offset SMEMT-EMT results for the $2S_{3/2}-1S_e$ state apparently underestimate the splitting in energy from the ground-state energy when compared with the corresponding experimental data. Figure 7 also indicates that the Γ_7-1S_e states with significant oscillator strength, which are split by $\approx\lambda$ from the ground state ($1\Gamma_8-1S_e$) for a wide range of dot radii, correspond to $S_{1/2}-1S_e$ states in the SMEMT-EMT scheme. This was con

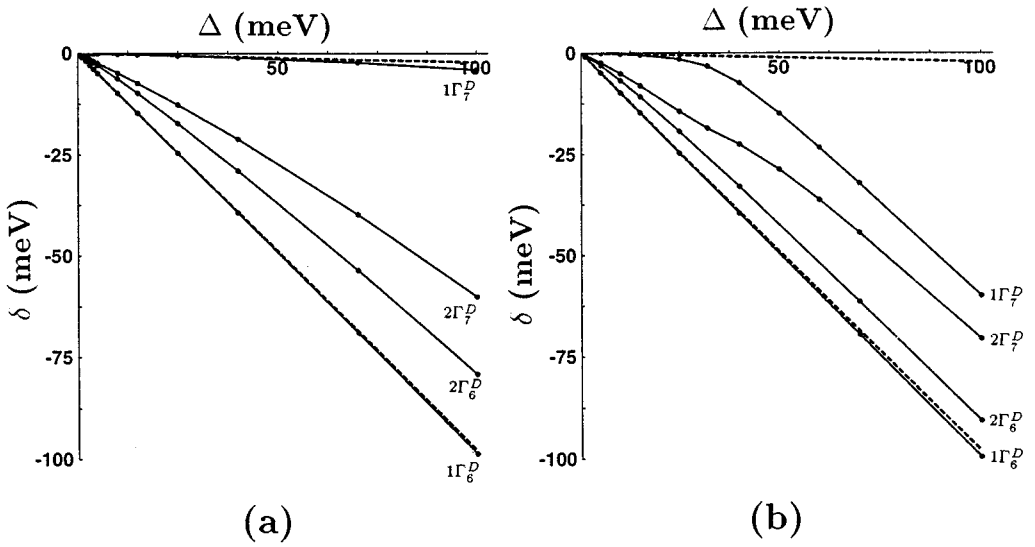

FIG. 5. The splitting $\delta = E_h(\Delta) - E_h(\Delta = 0)$ of the two lowest Γ_8 states ($1\Gamma_8$, $2\Gamma_8$) into ($1\Gamma_6^D$, $1\Gamma_7^D$) and ($2\Gamma_6^D$, $2\Gamma_7^D$) as a function of the crystal-field splitting Δ. The Luttinger parameters used are $\gamma_1 = 1.66$, $\gamma_2 = \gamma_3 = 0.41$, and $V_h = \infty$. The solid curves are interpolations of hexagonal EBOM results shown as dots. The dotted curves are calculated using Efros' expressions [Eq. (34)] with identical material parameters. The dotted curve with the smallest (largest) splitting δ corresponds to the $1\Gamma_7^D$ ($1\Gamma_6^D$) state. In (a) $R = 20.8$ Å and in (b) $R = 51.3$ Å.

firmed by changing the spin-orbit energy λ in the EBOM-EMT scheme and assuring that the $\Gamma_7 - 1S_e$ states with significant oscillator strength still were split by $\approx \lambda$ from the ground state. However, the infinite-offset models do not satisfactorily fit the other experimentally observed excited exciton states. From Fig. 7(b) we observe that the $2S_{3/2} - 2S_e$, $4S_{3/2} - 2S_e$, $1P_{3/2} - 1P_e$, and $1P_{1/2} - 1P_e$ SMEMT-EMT exciton states are also insufficient in this respect. Moreover, from the previous subsection we recall that the EBOM-EMT and SMEMT-EMT methods in the infinite-offset case predict too high ground-state energies. Below we therefore consider finite offsets in our EBOM-EMT scheme.

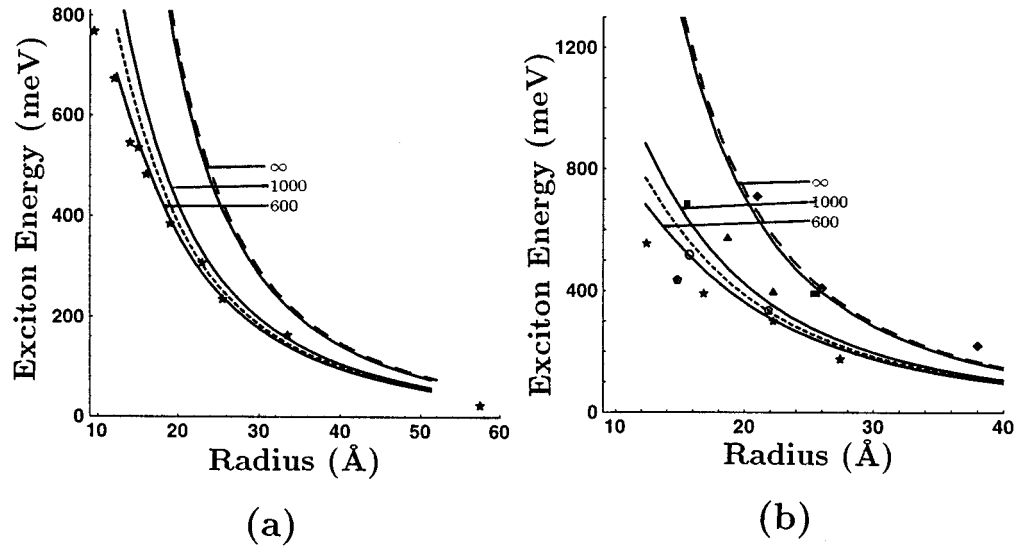

FIG. 6. Comparison with experiments for exciton ground-state energies for CdSe quantum dots. In (a) cubic EBOM-EMT and SMEMT-EMT results are compared with the experiments of Ref. 12 marked as stars. In (b) the same theoretical results are compared with numerous experimental results taken from Refs. 3 (open circle), 4 (square), 5 (star), 6 (rectangle), 8 (triangle), 9 (five-sided polygon), and 11 (diamond). The three solid curves in (a) and (b) correspond to EBOM-EMT results for $V_h = V_e = \infty$, 1000 meV, and 600 meV (marked with ∞, 1000, and 600). The dotted curves correspond to EBOM-EMT results for $V_h = \infty$ and $V_e = 600$ meV. The long-dashed curves correspond to infinite-offset results using SMEMT for the hole, EMT for the electron, and $V_{eh} = 1.8e^2/(4\pi\epsilon R)$ for the Coulomb interaction (Refs. 53 and 54). The parameters for CdSe in Table I with $\gamma_1 = 1.66$, $\gamma_2 = \gamma_3 = 0.41$ have been used. The band-gap energy has not been included in the exciton energies.

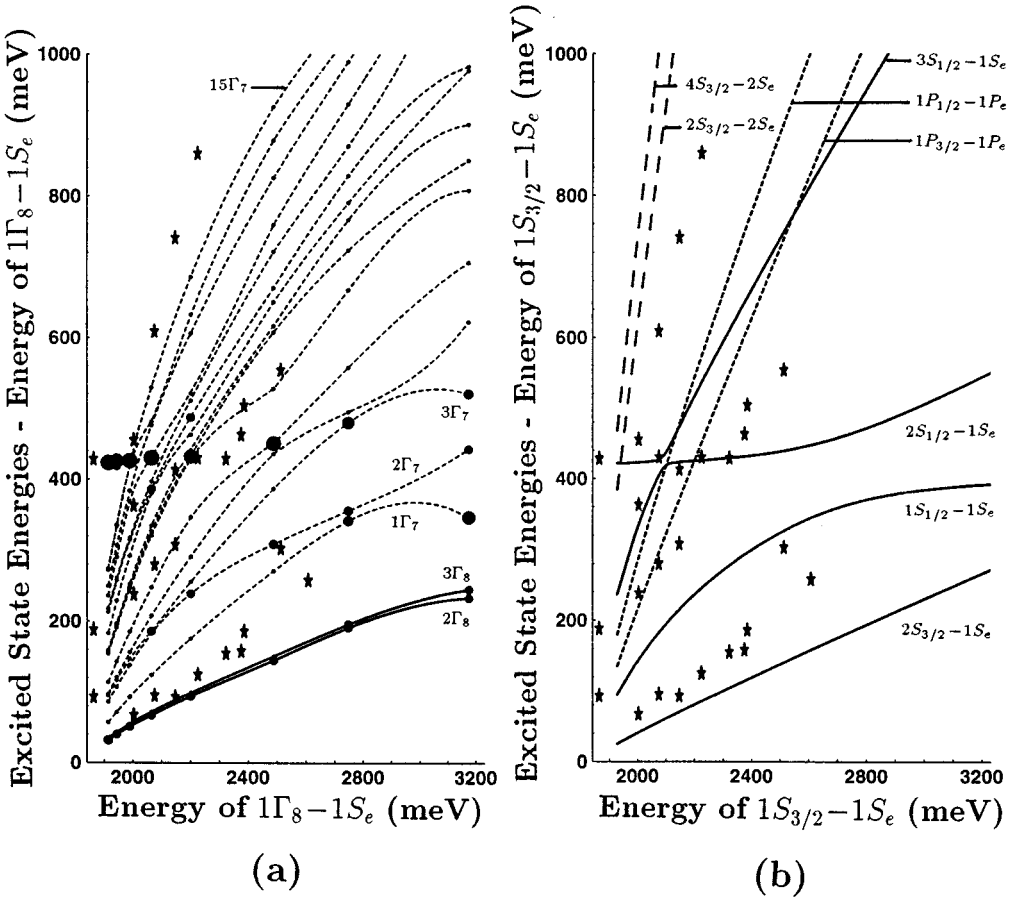

FIG. 7. Comparison with experiments for excited exciton states. The excited-state energies are shown as functions of the ground-state exciton energy. Experimental results of Norris *et al.* (Ref. 12) on CdSe quantum dots are marked as stars. (a) Comparison of even-parity infinite-offset cubic EBOM-EMT results with experimental results (Ref. 12). The parameters for CdSe in Table I with $\gamma_1=1.66$, $\gamma_2=\gamma_3=0.41$ have been used. Dotted curves correspond to the fifteen lowest Γ_7-1S_e states and solid curves to the $2\Gamma_8-1S_e$ and $3\Gamma_8-1S_e$ states. Filled dots outside curves correspond to other states with these symmetries and with large K. The curves are obtained by interpolating results for a discrete set of quantum dot radii ($R=14.9$, 17.8, 20.8, 27.1, 33.3, 39.3, 45.3, and 51.3 Å). The magnitude of the overlap factor K is indicated by the size of the filled dots: The largest filled dots correspond to $0.9\leqslant K<1$, the second largest filled dots correspond to $0.8\leqslant K<0.9$, etc. The radii of the filled dots are nearly two times larger for states with $0.9\leqslant K<1$ than for states with $0.01\leqslant K<0.1$. States with K less than 0.01 have been marked with the smallest filled dots, indicating that these states are optically weak. The Γ_8-1S_e states and some of the Γ_7-1S_e states are labeled on the graph. (b) Comparison of SMEMT-EMT results with experiments using $V_{eh}=1.8e^2/(4\pi\epsilon R)$ and $V_{eh}=1.7e^2/(4\pi\epsilon R)$ for transitions to the S_e and P_e levels, respectively (Refs. 53 and 54), with the same material parameters as in (a).

Figures 8(a) and 8(b) show the cubic EBOM-EMT exciton energy spectra with finite electron and hole offsets ($V_e=V_h=1000$ meV and $V_e=V_h=600$ meV) using the same material parameters as in Fig. 7(a). By comparison with the infinite-offset results we observe that for smaller offsets more states have a significant oscillator strength. Moreover, this effect is most pronounced for the smallest dots where the penetration into the barrier is most extensive. For both choices of offsets in Fig. 8 we find, as in the infinite-offset case, Γ_7-1S_e states with large overlap factors for states which are split by approximately the spin-orbit energy from the $1\Gamma_8-1S_e$ ground state. This supports the assignment of the experimentally observed exciton states with energies $\approx\lambda$ higher than the ground states for a wide range of radii as Γ_7-1S_e states. Such spin-orbit split-off states have also been observed in other experiments.[3,11]

In the finite-offset cases we also get good fits between the lowest band of experimentally observed states and the $2\Gamma_8-1S_e$ and $3\Gamma_8-1S_e$ states (especially for $V_e=V_h=1000$ meV).

The $1\Gamma_7-1S_e$ and $2\Gamma_7-1S_e$ states are found in the calculations to have large oscillator strengths, especially for small radii. Even though there are some experimental data points for the larger dots which are energetically close to the theoretical values for these states, the assignment of these to Γ_7-1S_e states is questionable. For instance, transitions involving higher-lying Γ_8 states [e.g., the $10\Gamma_8-1S_e$ transition seen in Fig. 8(a)] are also candidates. Norris *et al.*[12] suggested that the experimentally observed states in the range $\sim$ 200–300 meV above the ground state could correspond to the $1S_{1/2}-1S_e$ state. This would correspond to Γ_7-1S_e states in our scheme. We will, however, later in this

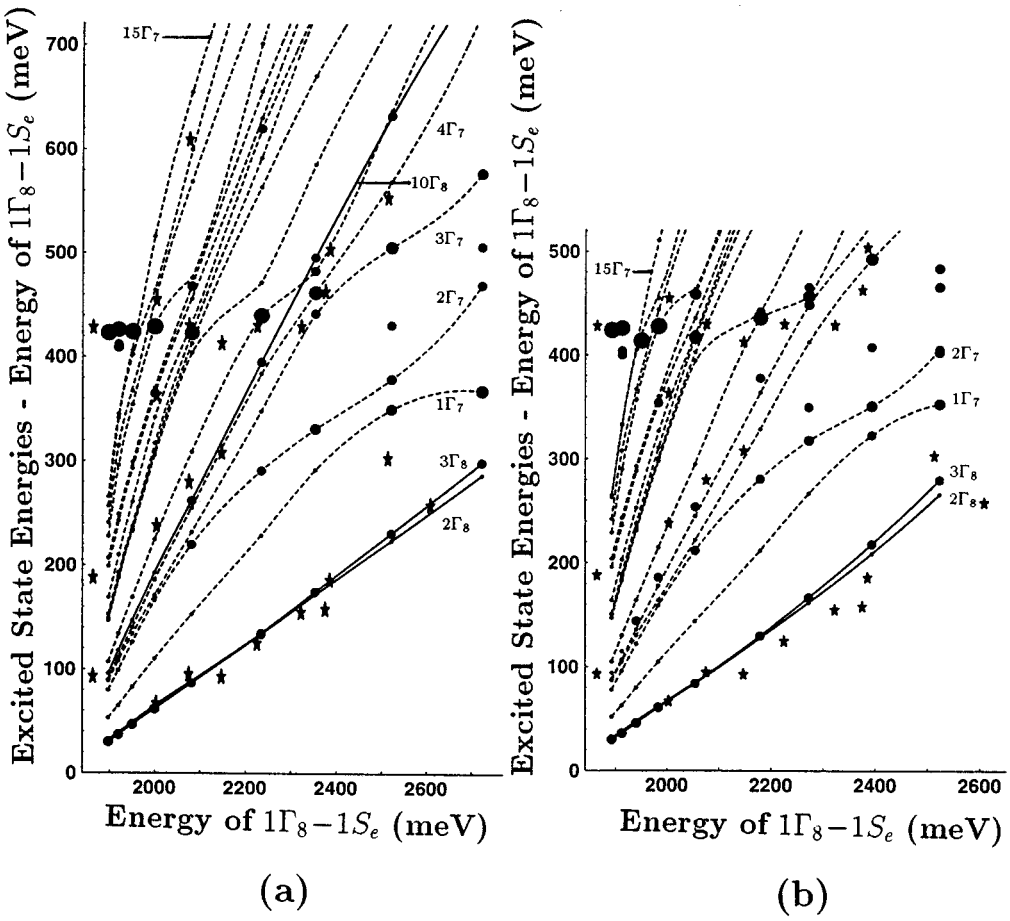

FIG. 8. (a) Same as Fig. 7(a) but $V_e=V_h=1000$ meV. Additional results for $R=12.3$ Å have been included. (b) Same as Fig. 8(a) but $V_e=V_h=600$ meV.

subsection show results which indicate that these experimental points may also correspond to the $1P_{3/2}-1P_e$ exciton state, which is expected to be optically strongly active.[11,34]

In Fig. 9(a) the cubic EBOM-EMT exciton energy spectrum for $V_e=600$ meV and $V_h=\infty$ is shown. Again we can assign (i) the Γ_7-1S_e transition with large oscillator strength (corresponding to $S_{1/2}-1S_e$ states) to the band of exciton states with energies $\approx\lambda=420$ meV above the ground-state energy, and (ii) the $2\Gamma_8-1S_e$ and $3\Gamma_8-1S_e$ transitions to the lower band of experimentally observed transitions. As for the previous choices of offsets, the assignment of the experimentally observed transitions between these two bands is not obvious. Note also that the results for $V_h=\infty, V_e=600$ meV in Fig. 9(a) are similar to the results for $V_h=V_e=600$ meV illustrating that the results are rather insensitive to the hole offset.

In Fig. 9(b) we have shown the corresponding results for the SMEMT-EMT scheme for $V_e=600$ meV and $V_h=\infty$. We have used the same perturbational results[53,54] for the Coulomb interaction as in Fig. 7(b) (even though these were derived for the infinite-offset case). In Fig. 9 curves for some of the states ($1P_{3/2}-1P_e$, $1P_{1/2}-1P_e$, $2S_{3/2}-2S_e$, and $4S_{3/2}-2S_e$) are not drawn for large ground-state energies ($1S_{3/2}-1S_e$), or, equivalently, for small dot radii. The reason is that the dot must have a minimum size to bind the electron when the electron offset is finite.[55]

From Fig. 9(b) it appears that with finite electron offset the $1P_{3/2}-1P_e$ state can account for the experimental data points observed between the $S_{1/2}-1S_e$ spin-orbit split-off states and the $2S_{3/2}-1S_e$ state for large radii. (The unbinding of the $1P_{3/2}-1P_e$ exciton in the model even occurs close to the dot radius for which this exciton state apparently vanishes in the experiment.) As discussed above, these experimental observations did not convincingly fit any of the even-parity states in our EBOM-EMT scheme.

When comparing Figs. 9(a) and 9(b) we see that the results for the exciton energy spectra using the SMEMT-EMT and the EBOM-EMT schemes give qualitatively similar results for the $2S_{3/2}-1S_e$ state and $2\Gamma_8-1S_e/3\Gamma_8-1S_e$ states. However, for small dot radii the EBOM-EMT results (which in contrast to the SMEMT-EMT scheme used here also incorporates the Coulomb interaction nonperturbatively) seem to fit the experimental data better.

In Fig. 10 we present cubic EBOM-EMT exciton energy spectra for a case where $\gamma_2\neq\gamma_3$, i.e., $\gamma_1=1.66$, $\gamma_2=0.41$, $\gamma_3=0.53$, and $V_e=V_h=1000$ meV. By comparing with Fig. 8(a), we see that the results for the exciton energies for $\gamma_2=\gamma_3$ and $\gamma_2\neq\gamma_3$ are qualitatively similar, even though the agreement with the $2\Gamma_8-1S_e$ and $3\Gamma_8-1S_e$ states apparently are slightly less good for the case with $\gamma_2\neq\gamma_3$. The main difference between Figs. 8(a) and 10 for the EBOM-EMT oscillator strengths is that there are more states with

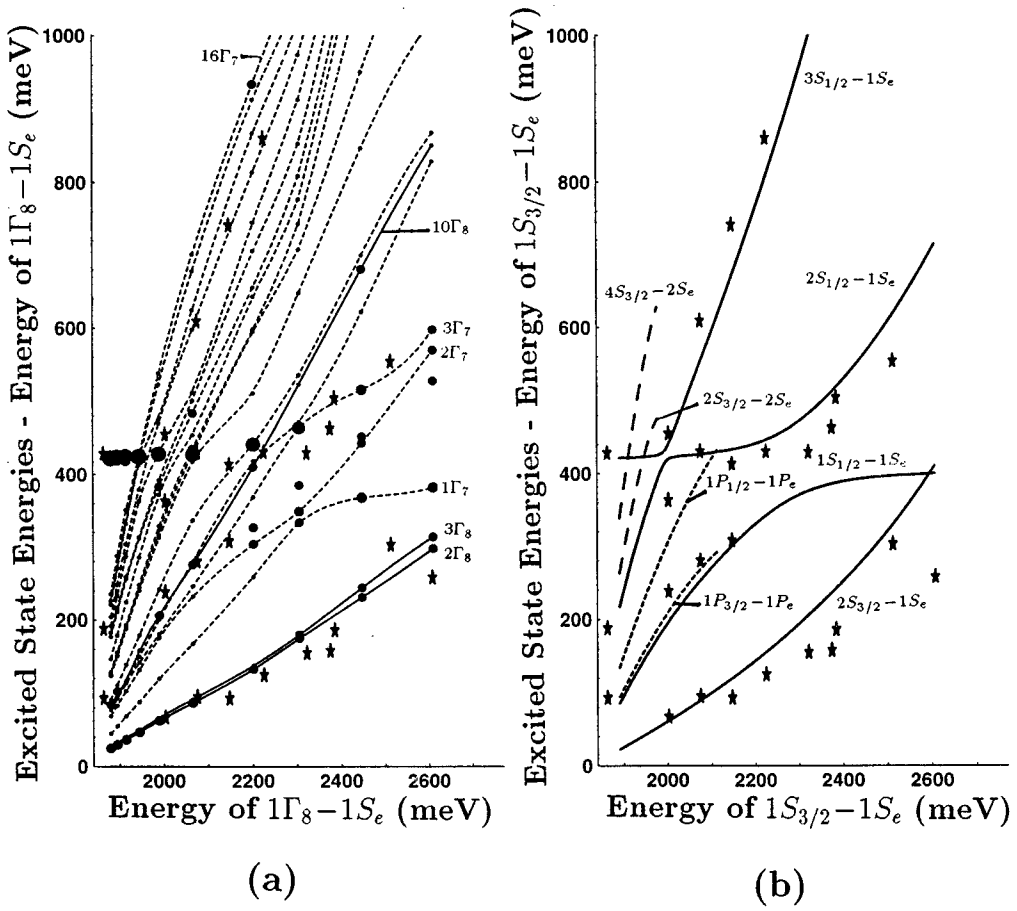

FIG. 9. (a) Same as Fig. 7(a) but $V_e=600$ meV. The calculations have been done for the same set of dot radii as in Fig. 7(a). In addition, results for $R=12.3$ Å and 57.5 Å have been included. (b) Same as Fig. 7(b) but $V_e=600$ meV.

non-negligible oscillator strengths for $\gamma_2\neq\gamma_3$ than for $\gamma_2=\gamma_3$. This is as expected since when cubic terms are included in the exciton Hamiltonian by setting $\gamma_2\neq\gamma_3$, more hole states will have contributions from $L=0$ than in the spherical case.[17,18]

Finally, we illustrate in Fig. 11 how the cubic EBOM-EMT overlap factor varies with the dot radius for the exciton case ($\epsilon=9.2\epsilon_0$) and the independent particle case ($\epsilon=\infty$) for both the infinite-offset case and for $V_e=V_h=600$ meV. In Fig. 11(a) we observe for the infinite-offset exciton case that the $1\Gamma_8-1S_e$ overlap factor decreases monotonically, while the $2\Gamma_8-1S_e$ overlap factor increases monotonically as the dot radius R increases and the confinement is reduced. In the infinite-offset case we also observe that the $1\Gamma_8-1S_e$ overlap is smaller and the $2\Gamma_8-1S_e$ overlap is larger for the exciton than for independent particles. However, for small radii the $1\Gamma_8-1S_e$ overlap approaches the same value for the independent-particle case and the exciton case. This is expected since the influence of the Coulomb interaction on the wave function disappears in this limit.

Efros[21] has calculated the overlap factor for the two lowest exciton states ($1S_{3/2}-1S_e$ and $2S_{3/2}-1S_e$) in the infinite-offset independent-particle SMEMT-EMT scheme, and his results are found to be in accordance with ours.

For the finite-offset case the $1\Gamma_8-1S_e$ overlap is generally smaller than for infinite offsets. The difference is large for small dot radii where the wave-function penetration into

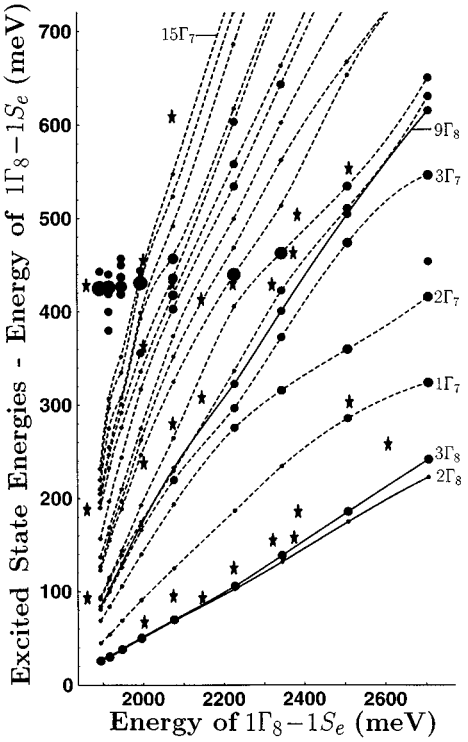

FIG. 10. Same as Fig. 8(a) ($V_e=V_h=1000$ meV), but the Luttinger parameters $\gamma_1=1.66$, $\gamma_2=0.41$, and $\gamma_3=0.53$ are used.

TABLE III. The overlap factor K for different cubic EBOM-EMT states and dot radii. The offsets are assumed infinite and $\gamma_1=1.66$, $\gamma_2=\gamma_3=0.41$. Other material parameters are taken from Table I. Overlap factors less than 10^{-3} have been rounded off to the nearest power of ten.

Exciton	Dot radius R (Å)							
state	14.9	17.8	20.8	27.1	33.3	39.3	45.3	51.3
$1\Gamma_8$	0.95	0.95	0.95	0.94	0.93	0.92	0.91	0.90
$2\Gamma_8$	0.013	0.027	0.041	0.058	0.072	0.084	0.093	0.10
$3\Gamma_8$	0.016	0.010	0.002	0.001	10^{-4}	10^{-5}	10^{-5}	10^{-5}
$4\Gamma_8$	10^{-4}	10^{-8}	10^{-5}	10^{-5}	10^{-6}	10^{-6}	10^{-7}	10^{-7}
$5\Gamma_8$	10^{-5}	10^{-5}	10^{-4}	10^{-4}	10^{-4}	10^{-4}	10^{-5}	0.001
$6\Gamma_8$	10^{-4}	10^{-5}	10^{-5}	10^{-5}	10^{-5}	10^{-6}	0.001	10^{-7}
$7\Gamma_8$	10^{-5}	10^{-6}	10^{-8}	10^{-7}	10^{-5}	10^{-5}	10^{-6}	10^{-6}
$8\Gamma_8$	10^{-4}	10^{-7}	10^{-7}	10^{-7}	10^{-7}	10^{-7}	10^{-6}	10^{-7}
$9\Gamma_8$	10^{-4}	10^{-5}	10^{-8}	10^{-5}	10^{-7}	10^{-8}	10^{-8}	10^{-8}
$10\Gamma_8$	10^{-5}	10^{-5}	10^{-8}	10^{-6}	10^{-4}	10^{-4}	10^{-8}	10^{-4}
$1\Gamma_7$	0.65	0.27	10^{-4}	10^{-4}	10^{-6}	10^{-8}	10^{-8}	10^{-7}
$2\Gamma_7$	0.035	0.14	0.18	0.036	0.001	10^{-6}	10^{-7}	10^{-7}
$3\Gamma_7$	0.29	0.58	10^{-4}	10^{-4}	0.010	0.004	0.002	0.001
$4\Gamma_7$	0.001	0.003	0.001	10^{-6}	10^{-5}	10^{-5}	10^{-5}	10^{-5}
$5\Gamma_7$	0.003	0.001	0.81	10^{-5}	10^{-6}	10^{-8}	10^{-8}	10^{-9}
$6\Gamma_7$	0.004	10^{-4}	10^{-4}	0.11	10^{-5}	10^{-8}	10^{-8}	10^{-8}
$7\Gamma_7$	0.001	0.001	10^{-4}	0.79	10^{-6}	10^{-7}	10^{-7}	10^{-7}
$8\Gamma_7$	10^{-5}	10^{-5}	10^{-5}	0.009	10^{-5}	10^{-6}	10^{-8}	10^{-8}
$9\Gamma_7$	0.002	0.003	0.005	0.001	0.002	10^{-5}	10^{-6}	10^{-9}
$10\Gamma_7$	0.001	10^{-4}	0.001	0.032	0.028	0.003	10^{-4}	10^{-5}
$11\Gamma_7$	0.001	10^{-4}	10^{-4}	0.001	0.001	10^{-4}	0.001	10^{-4}
$12\Gamma_7$	0.001	10^{-4}	0.001	10^{-4}	0.96	10^{-5}	10^{-6}	10^{-7}
$13\Gamma_7$	10^{-4}	10^{-4}	10^{-5}	10^{-6}	10^{-5}	10^{-6}	10^{-7}	10^{-7}
$14\Gamma_7$	0.004	10^{-5}	10^{-6}	10^{-7}	10^{-6}	10^{-6}	10^{-7}	10^{-7}
$15\Gamma_7$	0.011	10^{-6}	10^{-5}	10^{-6}	10^{-6}	10^{-6}	10^{-8}	10^{-9}
$16\Gamma_7$						0.99	10^{-6}	10^{-10}
$17\Gamma_7$						10^{-4}	10^{-6}	10^{-6}
$18\Gamma_7$						10^{-5}	10^{-6}	10^{-6}
$19\Gamma_7$						10^{-6}	0.004	10^{-4}
$20\Gamma_7$							0.19	0.002
$21\Gamma_7$							0.79	10^{-6}
$22\Gamma_7$							10^{-6}	10^{-4}
$23\Gamma_7$							10^{-6}	0.99

the barrier is large, while it is seen to nearly disappear for the largest dots considered where the barrier penetration is small.

The corresponding results for the Γ_7-1S_e states are less tidy, however, since the overlap factor changes rapidly when R varies. In Fig. 11(b) we show the overlap factor for the three lowest infinite-offset Γ_7-1S_e states which share most of the oscillator strength between themselves for small R. For $R>20$ Å the large oscillator strengths corresponding to the split-off $S_{1/2}-1S_e$ states are distributed to $n_h\Gamma_7-1S_e$ states with $n_h>3$.

C. Exciton binding energies

The difference between the exciton energy and the sum of the single-particle energies is commonly called the binding energy. The binding energy in the combined scheme with

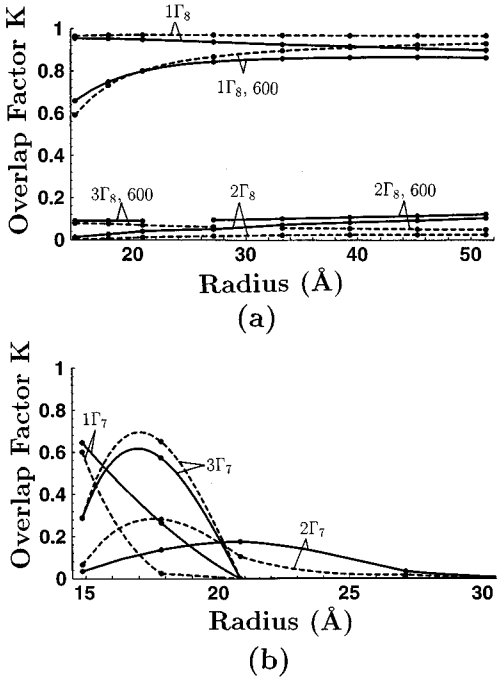

FIG. 11. Overlap factor K as a function of the dot radius for the exciton case (solid curves) and the independent-particle case (dotted curves). The parameters for CdSe in Table I with $\gamma_1=1.66$, $\gamma_2=\gamma_3=0.41$ have been used in the cubic EBOM-EMT scheme. In (a) the overlap factors for the optically important Γ_8-1S_e states are shown both for infinite offsets and finite offsets with $V_e=V_h=600$ meV (labeled 600 on the graph). The calculated values are shown by dots on the curves. Due to an avoided crossing for $V_e=V_h=600$ meV, between the $2\Gamma_8-1S_e$ and $3\Gamma_8-1S_e$ states in the range 20 Å $<R<33$ Å, these states have significant oscillator strength only for a limited range of dot radii and are thus not shown for all dot sizes. In (b) the overlap factor for the three lowest Γ_7-1S_e states is shown for infinite offsets.

cubic EBOM and EMT is plotted as a function of the dot radius R in Fig. 12. The parameters for CdSe in Table I with $\gamma_1=1.66$, $\gamma_2=\gamma_3=0.41$ have been used. In Figs. 12(a)–12(d) the binding energies for the states $1\Gamma_8-1S_e$, $2\Gamma_8-1S_e$, $1\Gamma_7-1S_e$, and $2\Gamma_7-1S_e$, respectively, are shown for various values of the electron and hole offsets. The binding energies for all the states shown in Fig. 12 are, as expected, found to decrease with decreasing electron and hole offsets due to the increased penetration of the wave function into the barrier when the offsets are lowered.

The curves for $V_h=V_e=600$ meV and for $V_h=\infty$, $V_e=600$ meV in Figs. 12(a)–12(d) show that there exists a radius for which the binding energy is maximal. This has previously been demonstrated for the exciton ground-state energy in both type-I quantum dots,[29] where both the electron and hole are confined to the dot, and in type-I_2^1 quantum dots,[56] where one of the particles is confined to the dot material, with the other free to move. In the limits $R\to 0$ and $R\to\infty$, the binding energy approaches the bulk binding energy of the barrier and dot material (which are identical in our calculations), respectively. It follows that the finite-offset binding energies will necessarily exhibit a maximum for a finite R. The curves for $V_h=V_e=1000$ meV in Fig. 12 would show a maximum if calculations for smaller dot radii had been included.

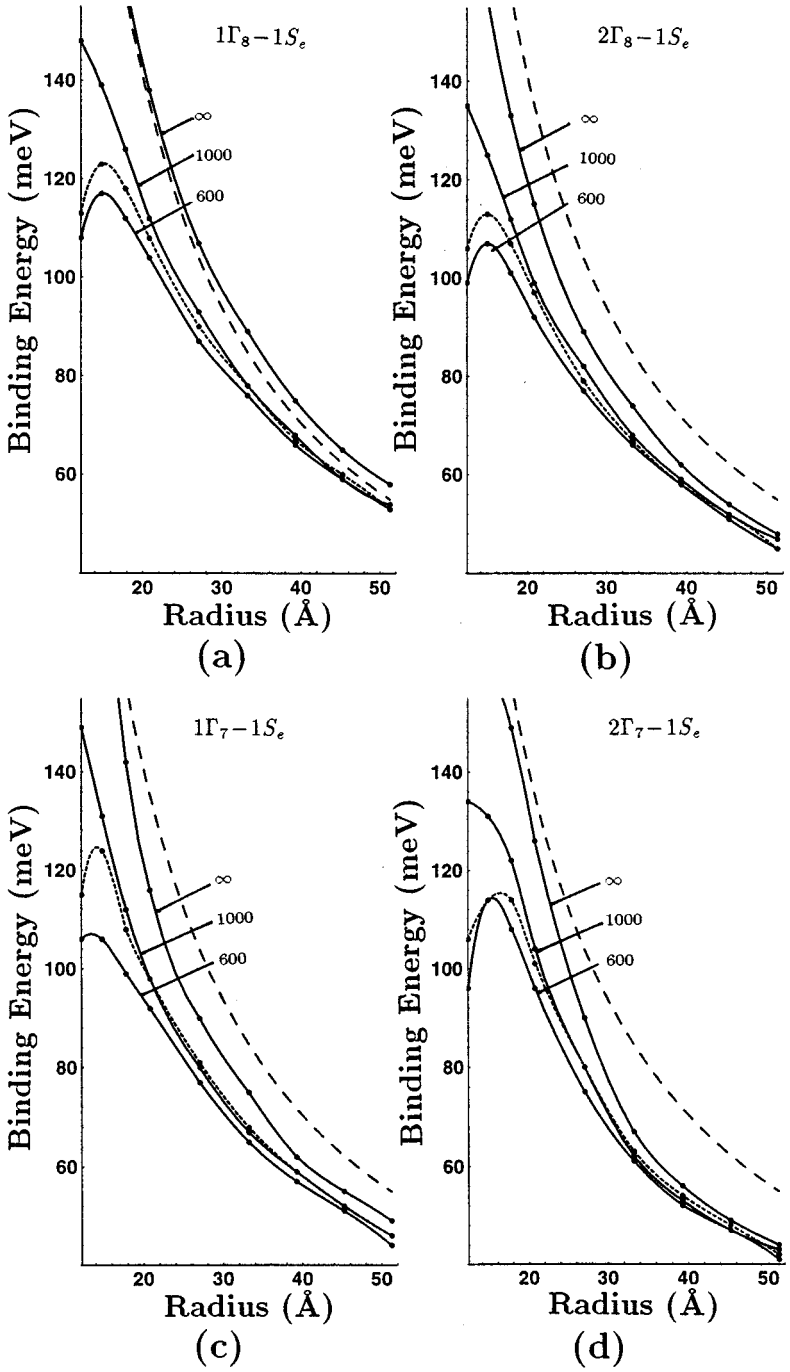

FIG. 12. Exciton binding energies in the cubic EBOM-EMT scheme for CdSe quantum dots as functions of the dot radius R for (a) $1\Gamma_8-1S_e$, (b) $2\Gamma_8-1S_e$, (c) $1\Gamma_7-1S_e$, and (d) $2\Gamma_7-1S_e$. The parameters for CdSe in Table I with $\gamma_1=1.66$, $\gamma_2=\gamma_3=0.41$ have been used. The three solid curves in (a)–(d) correspond to results for $V_h=V_e=\infty$, 1000 meV, and 600 meV (marked with ∞, 1000, and 600). The dotted curves correspond to results for $V_h=\infty$ and $V_e=600$ meV. The calculated values are shown as dots. The perturbative result (Refs. 53 and 54) $V_{eh}=1.8e^2/(4\pi\epsilon R)$ for the Coulomb interaction is shown as long-dashed curves.

For comparison we have also plotted the perturbative expression for the Coulomb interaction for the infinite-offset $1S_{3/2}-1S_e$ ground state $[V_{eh}=1.8e^2/(4\pi\epsilon R)]$, which was used in Ref. 11 and in our present SMEMT-EMT calculations. We observe in Fig. 12(a) a good agreement between our infinite-offset results for $1\Gamma_8-1S_e$ and the perturbative expression. However, it should be noted that the perturbative expression is seen to overestimate the infinite-offset binding energy for the $2\Gamma_8-1S_e$, $1\Gamma_7-1S_e$, and $2\Gamma_7-1S_e$ states.

D. Influence of crystal-field term

In Sec. IV B we investigated the influence of the crystal-field term due to the hexagonal structure of CdSe on the hole energy spectra. Here we study the effect of the crystal-field term on the exciton energies and the exciton overlap factors which determine the oscillator strength. The crystal-field term causes a splitting of the cubic Γ_8-1S_e exciton states into $\Gamma_6^D-1S_e$ and $\Gamma_7^D-1S_e$ exciton states. In Fig. 13 the overlap factor in the hexagonal EBOM-EMT scheme has been plotted as a function of the crystal-field splitting Δ for the optically most important states for a quantum dot with radius $R=20.8$ Å in the infinite-offset case. [The corresponding splitting of the Γ_8 hole states is shown in Fig. 5(a).]

In Fig. 13 we observe that the difference in overlap factors between the $1\Gamma_6^D-1S_e$ and $1\Gamma_7^D-1S_e$ states and between the $2\Gamma_6^D-1S_e$ and $2\Gamma_7^D-1S_e$ states, respectively,

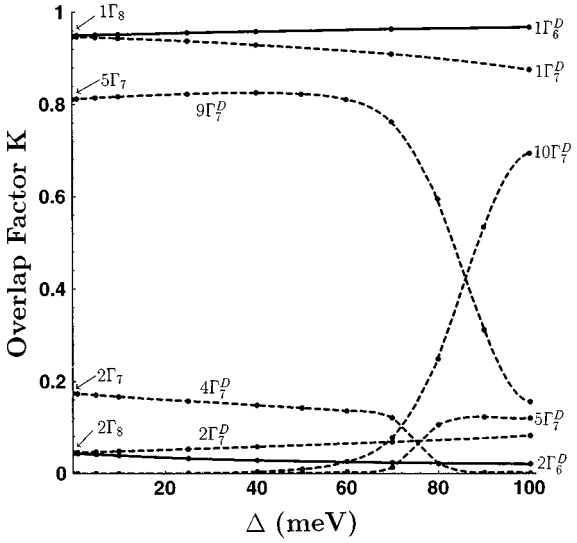

FIG. 13. Overlap factor K as a function of the crystal-field splitting Δ for the fixed dot radius $R=20.8$ Å for some of the optically most important states. The parameters for CdSe in Table I with $\gamma_1=1.66$, $\gamma_2=\gamma_3=0.41$, and $V_h=V_e=\infty$, have been used in the hexagonal EBOM-EMT scheme. The electronic part of the wave function corresponds in all cases to the $1S_e$ state. The calculated values are shown by dots on the curves. Note that there is no direct correspondence between the numbering of hexagonal and cubic EBOM states (Ref. 57).

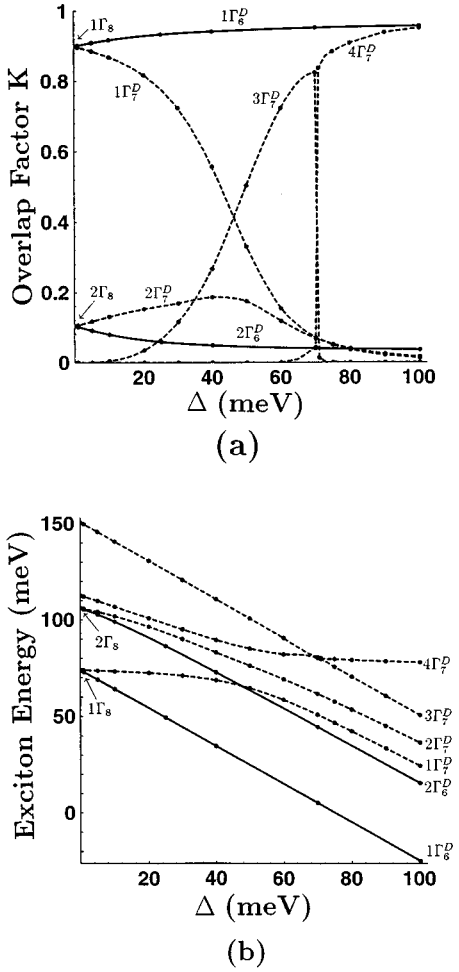

FIG. 14. Hexagonal EBOM-EMT results for the overlap factor K (a) and the corresponding exciton energies (b) as functions of the crystal-field splitting Δ for a fixed dot radius $R=51.3$ Å. Optically important cubic Γ_8-1S_e states ($\Delta=0$) are shown. The parameters for CdSe in Table I with $\gamma_1=1.66$, $\gamma_2=\gamma_3=0.41$, and $V_h=V_e=\infty$ have been used. The band-gap energy E_g has not been included in the exciton energies. Note that there is no direct correspondence between the numbering of hexagonal and cubic EBOM states (Ref. 57).

gradually increases when Δ is increased. However, no abrupt changes in the overlap factors for these two pairs of states occur in the range of Δ considered here. For the cubic Γ_7 states, on the other hand, we observe an interchange of oscillator strength due to avoided-crossing behavior between the $4\Gamma_7^D-1S_e$ and $5\Gamma_7^D-1S_e$ states and $9\Gamma_7^D-1S_e$ and $10\Gamma_7^D-1S_e$ states,[57] respectively, for Δ between 60 and 100 meV. The optically important $S_{1/2}-1S_e$ spin-orbit split-off states are seen to correspond to $9\Gamma_7^D-1S_e$ for Δ less than 60 meV. Figure 14(a) displays the same as Fig. 13 for the larger dot radius $R=51.3$ Å, and here a complicated pattern of avoided crossings is revealed for more modest values of Δ. This is not surprising since the crystal-field splitting is expected to have a large impact only when Δ is comparable to the hole confinement energies, which decrease with increasing dot radii. As seen in Fig. 1, the infinite-offset hole confinement energy for the Γ_8 ground state is 119 meV for $R=20.8$ Å while it is 22 meV for $R=51.3$ Å. The complicated behavior of the overlap factor for the large dot revealed in Fig. 14(a) is easier understood by also considering the exciton energy spectra shown in Fig. 14(b) [see also Fig. 5(b)]. The energies for the two lowest $\Gamma_6^D-1S_e$ states decrease roughly linearly with increasing Δ with no abrupt changes in the overlap factor. However, the energy spectra for the $\Gamma_7^D-1S_e$ states exhibit avoided-crossing behavior for approximately those values of Δ for which the overlap factor is susceptible to changes in Δ. The overlap factors and thus the oscillator strengths are seen to redistribute as Δ is increased to give more optical weight to higher $\Gamma_7^D-1S_e$ states. For $R=51.3$ Å we have not shown the effect of Δ on the Γ_7-1S_e states corresponding to the optically important $S_{1/2}-1S_e$ split-off states. For this large dot radius these split-off states correspond to a large number of energetically similar Γ_7-1S_e states which interchange optical strength as Δ is increased.

For CdSe, $\Delta\approx 25$ meV.[40] From Figs. 5 and 14(b) we see that for the $1\Gamma_8-1S_e$ and $2\Gamma_8-1S_e$ states, the splitting of absorption peaks due to the hole state splitting from the crystal-field term is expected to be less than Δ. The main contribution to the width of the absorption features in Ref. 12 comes almost certainly from sample inhomogeneities. This justifies our present approximation of neglecting the crystal-field term and using the cubic EBOM description when comparing our theory with the experimental absorption spectra by Norris *et al.* Note, however, that recent studies have indicated that in order to interpret *photoluminescence* spectra

both the crystal-field splitting term and the electron-hole exchange interaction must be taken into account.[36,58]

E. Choice of dielectric constants

In this paper we have used the static dielectric constant of CdSe, $\epsilon(0)=9.2\epsilon_0$, even though there is some controversy whether the static dielectric constant $\epsilon(0)$ or the optical dielectric constant $\epsilon(\infty)$ should be used.[1,47] For CdSe, the optical dielectric constant $\epsilon(\infty)\approx 6.0\epsilon_0$ (15 K).[40] The use of $\epsilon(\infty)$ instead of $\epsilon(0)$ would significantly increase the binding energies shown in Fig. 12. The effect on the exciton spectra in Figs. 7–10 would be less since the kinetic energy terms dominate the Coulomb energies for small quantum dots. The overlap factor is generally found to be not very sensitive to changes in the dielectric constant for our range of dot radii, and a choice of $\epsilon(\infty)$ instead of $\epsilon(0)$ would have small effects on the oscillator strengths for the dot radii and offsets considered here.

In our calculations we have neglected possible surface-polarization effects[59] by using the same value for the dielectric constant in the dot and barrier materials. Takagahara[59] has studied the effect of different dielectric constants in the dot and barrier in an infinite-offset model using single-band effective-mass theory for both the electron and the hole. In the strong-confinement limit the expression

$$E/E^*_{\mathrm{Ry}}=\pi^2\left(\frac{a^*_B}{R}\right)^2+A_1\frac{a^*_B}{R}+A_0 \tag{35}$$

was found for the ground-state energy. The coefficients A_0 and A_1, which are tabulated in Ref. 59, depend on the dielectric constant ratio $\epsilon_{\mathrm{dot}}/\epsilon_{\mathrm{barrier}}$. For the usual case with $\epsilon_{\mathrm{dot}}/\epsilon_{\mathrm{barrier}}=1$, Eq. (35) reduces to Kayanuma's well-known result Eq. (4). We have used Eq. (35) to study the influence of the surface polarization on the exciton ground-state energy using parameters suitable for CdSe ($a^*_B=50$ Å and $\epsilon_{\mathrm{dot}}=9.2\epsilon_0$). Due to the lack of reliable values for the dielectric constant for the matrix material used by Norris *et al.*,[12] we have studied the case with CdSe dots embedded in silicate glass where $\epsilon_{\mathrm{dot}}/\epsilon_{\mathrm{barrier}}\sim 3-4$. In this case the exciton ground-state energy will be larger than for $\epsilon_{\mathrm{dot}}/\epsilon_{\mathrm{barrier}}=1$. For dot radii between 10 and 50 Å, we find that the deviations between the calculated ground-state energies (not including the band-gap energy $E_g=1.84$ eV) for $\epsilon_{\mathrm{dot}}/\epsilon_{\mathrm{barrier}}=4$ and $\epsilon_{\mathrm{dot}}/\epsilon_{\mathrm{barrier}}=1$ vary from 2% for $R=10$ Å to 13% for $R=50$ Å. However, further theoretical work on the full exciton spectra which incorporates finite offsets and degenerate valence bands is needed to clarify the importance of surface polarization.

VI. CONCLUDING REMARKS

Our theoretical results from using the effective bond-orbital model (EBOM) for the hole and single-band effective-mass theory (EMT) for the electron in an iterative Hartree scheme, including the Coulomb interaction and finite offsets, have been found to account for most of the important features of the experimental absorption spectra for CdSe quantum dots obtained by Norris and co-workers. In addition to the exciton ground state ($1\Gamma_8-1S_e$), experimental states corresponding to $2\Gamma_8-1S_e$ and $3\Gamma_8-1S_e$ have been identified. Moreover, the band of experimental exciton states observed lifted with an energy close to the spin-orbit splitting $\lambda=420$ meV above the exciton ground state has been identified as Γ_7-1S_e spin-orbit split-off states with large oscillator strengths. The assignment of a collection of experimentally observed exciton states lifted $\sim$ 200–300 meV above the ground state is less clear, but several candidate states have been suggested (e.g., $1P_{3/2}-1P_e$).

TABLE IV. Cubic EBOM hole energies (in meV) of the ten lowest Γ_8 states and the five lowest Γ_7 states for $R=20.8$ Å, $\gamma_1=1.66$, $\gamma_2=\gamma_3=0.41$, and $V_h=\infty$. The rest of the material parameters are taken from Table I. $L=0,2,\ldots,L_{\max}$ cubic harmonics ${}^{L}K_i^{\Gamma\beta}$ are included.

Hole state	$L_{\max}=2$	$L_{\max}=4$	$L_{\max}=6$
$1\Gamma_8$	120	119	119
$2\Gamma_8$	242	242	241
$3\Gamma_8$	254	246	246
$4\Gamma_8$	440	363	361
$5\Gamma_8$	452	439	438
$6\Gamma_8$	528	467	455
$7\Gamma_8$	569	483	463
$8\Gamma_8$	764	498	494
$9\Gamma_8$	843	512	508
$10\Gamma_8$	864	526	521
$1\Gamma_7$	418	369	368
$2\Gamma_7$	469	418	416
$3\Gamma_7$	553	486	472
$4\Gamma_7$	763	523	520
$5\Gamma_7$	1057	553	552

The assumption of finite offsets has been found to be crucial in order to obtain quantitative agreement between our model and the experimental exciton spectra of Norris *et al.* Independent experimental assessment of the electron and hole offset is thus of significant interest.

The nonperturbative study of the effects of the crystal-field splitting Δ revealed patterns of avoided crossings accompanied with redistribution of oscillator strengths between different states. In CdSe, $\Delta\approx 25$ meV and the main contribution to the width of the absorption peaks in Ref. 12 is expected to come from sample inhomogeneities and not from the crystal-field splitting term.

For the largest dot radii considered, the EBOM hole confinement energies are in excellent agreement with results from the spherical multiband effective-mass theory (SMEMT). However, for small dot radii the EBOM predicts lower confinement energies, apparently in better agreement with experiments. The EBOM confinement energies are also closer to results from the empirical tight-binding method and the empirical pseudopotential method.[23–26,29]

In other calculational schemes that incorporate the complicated valence-band structure, the Coulomb interaction is only included perturbatively. Often the strong-confinement result for the Coulomb energy for the infinite-offset exciton ground state is used, even for excited exciton states. As re-

vealed by the binding energies shown in Fig. 12, this may give inaccurate results for all exciton states for systems with finite offsets and for excited exciton states in the infinite-offset case.

ACKNOWLEDGMENTS

We thank P. C. Hemmer for useful discussions and for a careful reading of the manuscript, and F. B. Pedersen for useful remarks. One of us (U.E.H.L.) is grateful to Norges Forskningsråd for support. This work has received support from The Research Council of Norway (Programme for Supercomputing) through a grant of computing time. The use of the Cray Research Inc. Y-MP4D/464 and the Cray Research Inc. J90 at the Norwegian University of Science and Technology is acknowledged.

APPENDIX

In the cubic EBOM calculations reported here cubic harmonics corresponding to $L=0$, 2, 4, and 6 have been included in the hole basis functions to describe the lowest hole states. This is expected to be a good approximation for S, D, and G states. The relative importance of the contributions from different L's is illustrated in Table IV by means of a special example: the first ten Γ_8 hole states and the first five Γ_7 states have been calculated for the dot radius $R=20.8$ Å.

In Sec. IVA the $1\Gamma_8$ state was identified as the $1S_{3/2}$ state and should have its main contributions from $L=0$ and $L=2$. From Table IV we see that, as expected, the hole energy for the $1\Gamma_8$ state changes by only 1 meV when $L_{\max}$ is increased from 2 to 6. We observe that most states have small changes in energies when $L_{\max}$ is increased from 4 to 6, and this contributes to justifying that cubic harmonics with $L \geqslant 8$ can be neglected in our calculations.

*Present address: Institutt for tekniske fag, Norges Landbrukshøgskole, N-1432 Ås, Norway.

[1] A. D. Yoffe, Adv. Phys. **42**, 173 (1993).
[2] U. Woggon and S. V. Gaponenko, Phys. Status Solidi B **189**, 285 (1995).
[3] M. G. Bawendi, W. L. Wilson, L. Rothberg, P. J. Carroll, T. M. Jedju, M. L. Steigerwald, and L. E. Brus, Phys. Rev. Lett. **65**, 1623 (1990).
[4] U. Woggon, M. Müller, U. Lembke, I. Rückmann, and J. Cesnulevicius, Superlatt. Microstruct. **9**, 245 (1991).
[5] N. Nogami, S. Suzuki, and K. Nagasaka, J. Non-Cryst. Solids **135**, 182 (1991).
[6] S. H. Park, R. A. Morgan, Y. Z. Hu, M. Lindberg, S. W. Koch, and N. Peyghambarian, J. Opt. Soc. Am. B **7**, 2097 (1990).
[7] N. Chestnoy, R. Hull, and L. E. Brus, J. Chem. Phys. **85**, 2237 (1986).
[8] A. P. Alivisatos, A. L. Harris, N. J. Levinos, M. L. Steigerwald, and L. E. Brus, J. Chem. Phys. **89**, 4001 (1988).
[9] N. F. Borrelli, D. W. Hall, H. J. Holland, and D. W. Smith, J. Appl. Phys. **61**, 5399 (1987).
[10] G. Hodes, A. Albu-Yaron, F. Decker, and P. Motisuke, Phys. Rev. B **36**, 4215 (1987).
[11] A. I. Ekimov, F. Hache, M. C. Schanne-Klein, D. Ricard, C. Flytzanis, I. A. Kudryavtsev, T. V. Yazeva, A. V. Rodina, and Al. L. Efros, J. Opt. Soc. Am. B **10**, 100 (1993).
[12] D. J. Norris, A. Sacra, C. B. Murray, and M. G. Bawendi, Phys. Rev. Lett. **72**, 2612 (1994).
[13] C. B. Murray, C. R. Kagan, and M. G. Bawendi, Science **270**, 1335 (1995).
[14] Al. L. Efros and A. L. Efros, Fiz. Tekh. Poluprovodn. **16**, 1209 (1982) [Sov. Phys. Semicond. **16**, 772 (1982)].
[15] Y. Kayanuma, Phys. Rev. B **38**, 9797 (1988).
[16] Y. Kayanuma and H. Momiji, Phys. Rev. B **41**, 10 261 (1990).
[17] N. O. Lipari and A. Baldereschi, Phys. Rev. Lett. **25**, 1660 (1970).
[18] A. Baldereschi and N. O. Lipari, Phys. Rev. B **8**, 2697 (1973).
[19] J.-B. Xia, Phys. Rev. B **40**, 8500 (1989).
[20] P. C. Sercel and K. J. Vahala, Phys. Rev. B **42**, 3690 (1990).
[21] Al. L. Efros, Phys. Rev. B **46**, 7448 (1992).
[22] Al. L. Efros, Physica B **185**, 575 (1993).
[23] Y. Wang and N. Herron, J. Phys. Chem. **91**, 257 (1987); **92**, 4988 (1988); **95**, 525 (1991); Phys. Rev. B **42**, 7253 (1990).
[24] P. E. Lippens and M. Lannoo, Phys. Rev. B **39**, 10 935 (1989); **41**, 6079 (1990); Semicond. Sci. Technol. **6**, A157 (1991).
[25] M. V. Rama Krishna and R. A. Friesner, Phys. Rev. Lett. **67**, 629 (1991); J. Chem. Phys. **95**, 8309 (1991).
[26] L.-W. Wang and A. Zunger, Phys. Rev. B **53**, 9579 (1996).
[27] Y.-C. Chang, Phys. Rev. B **37**, 8215 (1988).
[28] G. T. Einevoll and Y.-C. Chang, Phys. Rev. B **40**, 9683 (1989).
[29] G. T. Einevoll, Phys. Rev. B **45**, 3410 (1992).
[30] S. V. Nair, L. M. Ramaniah, and K. C. Rustagi, Phys. Rev. B **45**, 5969 (1992).
[31] L. M. Ramaniah and S. V. Nair, Phys. Rev. B **47**, 7132 (1993).
[32] J. M. Luttinger and W. Kohn, Phys. Rev. **97**, 869 (1955).
[33] E. O. Kane, J. Phys. Chem. Sol. **1**, 249 (1957).
[34] G. B. Grigoryan, E. M. Kazaryan, Al. L. Efros, and T. V. Yazeva, Fiz. Tverd. Tela (Leningrad) **32**, 1772 (1990) [Sov. Phys. Solid State **32**, 1031 (1990)].
[35] G. L. Bir and G. E. Pikus, *Symmetry and Strain-Induced Effects in Semiconductors* (Wiley, New York, 1975).
[36] M. Nirmal, D. J. Norris, M. Kuno, M. G. Bawendi, Al. L. Efros, and M. Rosen, Phys. Rev. Lett. **75**, 3728 (1995).
[37] G. T. Einevoll, D. S. Citrin, and Y.-C. Chang, Phys. Rev. B **44**, 8068 (1991).
[38] G. T. Einevoll and Y.-C. Chang, Phys. Rev. B **41**, 1447 (1990).
[39] See E. A. Hylleraas, *Mathematical and Theoretical Physics* (Wiley, New York, 1970), Vol. 1, p. 109.
[40] *Physics of II-VI and I-VII Compounds, Semimagnetic Semiconductors*, edited by O. Madelung, M. Schultz, and H. Weiss, Landolt-Börnstein, New Series, Group III, Vol. 17, Pt. b (Springer, Berlin, 1982); *Intrinsic Properties of Group IV Elements and III-V, II-VI and I-VII Compounds*, edited by O. Madelung, Landolt-Börnstein, New Series, Group III, Vol. 22, Pt. a (Springer, Berlin, 1987).
[41] G. F. Koster, J. O. Dimmock, R. G. Wheeler, and H. Statz, *Properties of the Thirty-Two Point Groups* (MIT Press, Cambridge, MA, 1963).
[42] J. C. Slater and G. F. Koster, Phys. Rev. **94**, 1498 (1954).
[43] F. C. Von der Lage and H. A. Bethe, Phys. Rev. **71**, 612 (1947).
[44] Al. L. Efros and A. V. Rodina, Phys. Rev. B **47**, 10 005 (1993).
[45] C. H. Henry and K. Nassau, Phys. Rev. B **1**, 1628 (1970).
[46] L. C. Andreani and A. Pasquarello, Europhys. Lett. **6**, 259 (1988).

[47] L. Bányai, P. Gilliot, Y. Z. Hu, and S. W. Koch, Phys. Rev. B **45**, 14 136 (1992).

[48] See C. Weisbuch and B. Vinter, *Quantum Semiconductor Structures* (Academic, San Diego, 1991), p. 15.

[49] $m_{\|A}$ is found from the exciton effective mass combined with $m_e = 0.13m_0$. $m_{\perp A} = 0.375m_0$ is an average of a value of $m_{\perp A}$ found from the exciton mass and a separately listed value in Ref. 40.

[50] P. Lawaetz, Phys. Rev. B **4**, 3460 (1971).

[51] L. M. Ramaniah and S. V. Nair, Physica B **212**, 245 (1995).

[52] In Refs. 17 and 18 it was found that when $\gamma_2 = \gamma_3$ the cubic terms vanish both without spin-orbit coupling ($\lambda = 0$) and in the limit of infinite spin-orbit coupling ($\lambda = \infty$).

[53] Al. L. Efros and A. V. Rodina, Solid State Commun. **72**, 645 (1989).

[54] G. B. Grigoryan, A. V. Rodina, and Al. L. Efros, Fiz. Tverd. Tela (Leningrad) **32**, 3512 (1990) [Sov. Phys. Solid State **32**, 2037 (1990)].

[55] F. B. Pedersen, U. E. H. Laheld, and P. C. Hemmer, Superlatt. Microstruct. **17**, 431 (1995); **18**, 332(E) (1995).

[56] U. E. H. Laheld, F. B. Pedersen, and P. C. Hemmer, Phys. Rev. B **52**, 2697 (1995).

[57] Note that the labeling of the hole states ($n_h\Gamma_7^D$) refers to the numbering of hole states in our hexagonal EBOM method which includes angular basis functions corresponding to angular momentum $L = 0$ and 2, only. Since in contrast to the cubic EBOM scheme $L = 4$ and 6 are not included, there is no direct correspondence between the numbering of hexagonal and cubic states.

[58] M. Chamarro, C. Gourdon, P. Lavallard, O. Lublinskaya, and A. I. Ekimov, Phys. Rev. B **53**, 1336 (1996).

[59] T. Takagahara, Phys. Rev. B **47**, 4569 (1993).